PAPER • OPEN ACCESS

Super-X and conventional divertor configurations in MAST-U ohmic L-mode; a comparison facilitated by interpretative modelling

To cite this article: D. Moulton *et al* 2024 *Nucl. Fusion* **64** 076049

OPEN ACCESS
IOP Publishing | International Atomic Energy Agency
Nuclear Fusion
Nucl. Fusion **64** (2024) 076049 (31pp)
https://doi.org/10.1088/1741-4326/ad4f9c

Super-X and conventional divertor configurations in MAST-U ohmic L-mode; a comparison facilitated by interpretative modelling

D. Moulton[1,*], J.R. Harrison[1], L. Xiang[1], P.J. Ryan[1], A. Kirk[1], K. Verhaegh[1], T.A. Wijkamp[2,3], F. Federici[4], J.G. Clark[1] and B. Lipschultz[5]

[1] UKAEA, Culham Science Centre, Abingdon OX14 3DB, United Kingdom of Great Britain and Northern Ireland
[2] DIFFER—Dutch Institute for Fundamental Energy Research, De Zaale 20, 5612 AJ Eindhoven, Netherlands
[3] Department of Applied Physics, Eindhoven University of Technology, Eindhoven 5600 MB, Netherlands
[4] Oak Ridge National Laboratory, Oak Ridge, TN 37831, United States of America
[5] York Plasma Institute, University of York, York, United Kingdom of Great Britain and Northern Ireland

E-mail: david.moulton@ukaea.uk

Received 2 January 2024, revised 2 April 2024
Accepted for publication 23 May 2024
Published 11 June 2024

Abstract

Measurements are presented, alongside corresponding interpretative SOLPS-ITER simulations, of the first MAST-U experiments comparing ohmically heated L-mode fuelling scans in Conventional divertor (CD) and Super-X divertor (SXD) configurations. In experiment, at comparable outer mid-plane separatrix electron density, $n_{e,\mathrm{sep,OMP}}$, the maximum lower outer target heat load was found to be a factor 16 ± 7 lower in SXD compared to CD. In simulation, a factor 26.8 reduction was found (slightly higher than the experimental range), suggesting an additional reduction in SXD compared to the factor 9.3 expected from geometric considerations alone. According to the simulations, this additional reduction in the SXD is due to a net radial transport of the energy remaining downstream of the $T_e = 5$ eV location. This energy is carried out of the critical (highest heat load) flux tube by deuterium atoms, demonstrating the importance of a longer legged divertor which provides space for this to occur. Importantly, in both simulation and experiment, the SXD has minimal impact on the upstream n_e and T_e profiles. Spectral inferences of detachment front movement in SXD compare well between simulation and experiment. In regions of high magnetic field gradient, the parallel movement of the front towards the X-point becomes less sensitive to increasing $n_{e,\mathrm{sep,OMP}}$, in qualitative agreement with simplified models and previous predictive simulations. Additional aspects, regarding the target ion flux rollover, upstream separatrix temperature and drift effects, are also presented and discussed.

---

[*] Author to whom any correspondence should be addressed.

1741-4326/24/076049+31$33.00 Printed in the UK

Keywords: MAST-U, Super-X, SOLPS, divertor design, experimental comparison, L-mode

(Some figures may appear in colour only in the online journal)

1. Introduction

The recently upgraded spherical tokamak MAST-U [1, 2] provides an important test bed to assess the utility of the Super-X divertor (SXD) configuration for future fusion reactors. In an SXD [3], the poloidally flared geometry of an X-divertor (XD) [4] is moved to higher major radius in order to reduce the target parallel energy flux density and promote detachment onset. The SXD is particularly applicable to low aspect ratio spherical tokamak (ST) reactors, since the achievable increase in major radius from divertor entrance to target is larger than for higher aspect ratio machines. Even for high aspect ratio reactors such as DEMO, however, an SXD has been predicted to result in significant benefits [5]. Irrespective of aspect ratio, an SXD comes at considerable additional cost since it occupies a large portion of the precious volume inside the toroidal field coils. When designing a reactor, it is therefore important to quantify the performance improvement that an SXD would provide, compared to a conventional divertor (CD).

In order to develop such a quantitative and predictive capability, one must first understand the benefit provided by an SXD on current machines like MAST-U. In this paper, we present the first such comparison of two fuelling scans, in CD and SXD, for ohmic L-mode plasmas from the first MAST-U campaign[6]. To aid interpretation of the experimental data, interpretative modelling with the boundary code SOLPS-ITER [6, 7] is presented and compared to the experimental results. In addition to improved interpretation, this allows for an assessment of the code's ability to reproduce measured improvements in the SXD configuration on current machines, providing an increased level of confidence in the code to make predictions for future ST reactors.

Measures of SXD performance improvement, relative to CD, typically relate to the additional exhaust-compatible upstream operational space that it provides. This can be defined according to the upstream impurity concentration, the upstream separatrix density, and/or the separatrix power required for tolerable[7] exhaust (lower values of the first two and higher values of the last represent an increase in operational space). In the simple analytic models of SXD performance improvement developed in [8, 9], tolerable exhaust is assumed to occur when all of the plasma energy flux entering the divertor is radiated before it reaches the target, which itself is defined in the model as detachment onset[8]. In a real reactor, however, the transition from an intolerable to a tolerable exhaust scenario will likely be gradual (see, for example, the gradual reduction in peak total target heat load predicted for ITER, as a function of neutral pressure [12]). As a result, various definitions for detachment onset in experiment exist (including when the ion target flux starts to decrease, or when the plasma temperature at the target reaches ∼5 eV, or when certain radiation lines start to move off the target), but none of them are in exact correspondance with the operational space.

Regarding ion target flux rollover, SOLPS simulations which isolate the effect of increased target major radius in a simplified 'box' geometry, have shown a reduction in the required upstream density for rollover [13], in quantitative agreement with the simplified model mentioned above [8]. In experiment, however, no reduction in the upstream density required for ion target flux rollover was observed on TCV as the outer strike point was moved to higher major radius [14]. This discrepancy was attributed to a concomitant change in the target poloidal inclination angle to the separatrix α_{tilt}, resulting in higher neutral leakage from the divertor which fully cancelled the expected improvement in detachment access [15]. In predictive modelling of MAST-U, a reduced sensitivity to α_{tilt} was found, likely due to improved neutral baffling [16] (in baffled divertors, upstream parallel flows tend to be weaker; such flows can otherwise lead to deviations from the expected impact of target major radius predicted by a conduction-only two point model [17]). Nevertheless, to avoid such confounding effects in the study presented here, we kept α_{tilt} the same in CD and SXD configurations.

In this work, an experimental comparison of the ion flux rollover in CD vs SXD proved difficult due to strike point splitting at low density (section 2). However, as alluded to above, ratios of the upstream density required for target flux rollover are not necessarily indicative of the utility of an SXD, since target flux rollover alone does not guarantee an acceptable target heat load. Perhaps a more direct measure of the relative

---

[6] Additional complexity is added by the transition to H-mode and the presence of seeded impurities which, although entirely relevant to future reactors, are not the focus of this initial study.

[7] In terms of target heat loads, impurity sputtering and helium pumping.

[8] The same assumption was also recently employed in an analytic integrated model to guide reactor design choices [10, 11]. Note that the detachment 'window' in [8], defined as the set of upstream parameters for which onset has occurred but the detachment front has not yet reached the X-point, is synonymous with the operational space. In that model, since the front position is independent of the magnetic configuration downstream of it, the increase in detachment window (i.e. operational space) for an SXD is entirely governed by the ease with which onset occurs (assuming SXD and CD have the same magnetic geometry upstream of the X-point).

performance of SXD vs. CD is the peak target heat load reduction factor for the same upstream conditions. In the comparable region where neither configuration had strike point splitting, this factor was considerable (26.8 in the interpretative simulations and slightly lower in experiment; see section 4.5). This is a factor 2.9 more than expected from geometric considerations alone (due to increased target major radius and poloidal flux expansion), suggesting a significant additional advantage to the SXD due to neutral dissipation in the long leg.

Another important measure of SXD performance is the sensitivity of the detachment front to changes in the upstream plasma. A local region of low sensitivity is desirable in the divertor, in order to keep the front at a position where target loads and helium pumping are acceptable, without unwanted radiation or impurity contamination in the core. In addition, wall structures surrounding that position can be fortified against radiation loads. It is therefore important that the SOLPS-ITER code is capable of reproducing the experimental movement of detachment fronts, if it is to be used for predicting that same behaviour in future reactors. In this paper, for the first time, we show a direct comparison between experiment and SOLPS-ITER simulations of the detachment front sensitivity in the MAST-U SXD. Encouragingly, the code is able to quantitatively reproduce the detachment front movement (as measured by the trailing edge of the molecular Fulcher emission; section 4.6.4), at least in the unseeded, low power L-mode plasmas studied here.

The paper is organised as follows. In sections 2 and 3 we present an overview of the experiments and their associated simulations, respectively. The results of the experiments and simulations are presented alongside each other in section 4, with discussion following in section 5. Finally, we conclude in section 6.

2. Experimental setup and overview

Ohmically heated L-mode plasmas were generated with CD and SXD outer divertor configurations, in double null geometry, with an on-axis toroidal field of $B_t = 0.5$ T and a plasma current of $I_p = 600$ kA. In section 3, which discusses the simulation setup, we provide a comparison of the two magnetic equilibria (see figure 2, where the simulation grids based on those equilibria are shown). Note that, in light of the previously observed confounding nature of the target tilt angle in the poloidal plane relative to the separatrix (α_{tilt}) [15], this angle was held constant in the two configurations. Some important parameters are shown for each shot as a function of time in figure 1, with bold lines showing the chosen time windows for analysis.

Figures 1(*a*) and (*b*) show the fuelling profiles, with the resulting line averaged density shown in figures 1(*c*) and (*d*). The CD database comprises 4 shots with fuelling ramps in each, while the SXD database comprises 10 shots with (different) fixed fuelling in each. Deuterium gas was injected from the high field side (HFS), near the mid-plane. The ohmic heating power is given in figures 1(*e*) and (*f*), with the approximate radiation from the portion of the core not covered by the simulation grids (calculated from infra-red video bolometry, IRVB) shown for comparison[9]. Figures 1(*g*) and (*h*) show δr_{sep}, the separation between primary and secondary separatrices mapped to the outer mid-plane (OMP); negative values correspond to a lower primary X-point.

The last two rows, figures 1(*i*)–(*l*), show the surface normal heat loads derived from infra-red thermography, as a function of time and major radius, for four example shots. The double peaked nature of the radial profile observed for shots 45 470 and 45 459 in figures 1(*i*) and (*j*), respectively, is termed ‘strike point splitting’, and is thought to be the result of intrinsic error field penetration [18]. The threshold for error field penetration decreases with plasma density, so that strike point splitting is observed for all but the highest density shots in this database (45469 in CD configuration, and 45463 and 454644 in SXD). The same plots are shown for 45 469 and 45 463 in figures 1(*k*) and (*l*), respectively; those do not exhibit splitting. As will be discussed in more detail, the strike point splitting does complicate the analysis[10].

3. Simulation setup and overview

Interpretative SOLPS-ITER simulations were run using the ‘B2SOLPS5.2’ set of plasma equations [19], themselves based on the Braginskii fluid equations [20]. For each simulation, the EIRENE Monte-Carlo kinetic code [21] was used to calculate the neutral-plasma interactions, and iterated together with the plasma solver until a steady state, converged solution was achieved. Version 3.0.8 of the SOLPS-ITER code package was employed, with the same equation settings and boundary condition types as previously used in [22]. Unless otherwise stated, all drift terms were turned on. Inputs to the code were as follows:

- A single grid for each of the CD and SXD configurations was created using the CARRE module [23] within the SOLPS-ITER code suite, see figure 2. The CD grid was based on the experimental equilibrium for shot 45470 at 0.42 s, while the SXD grid was based on shot 45456 at 0.445 s. The equilibria were symmetrised about the mid-plane before gridding, forcing the simulations to be perfectly connected double null. We observe from figures 1(*i*) and (*j*) that there is some drift in $|\delta r_{\text{sep}}|$ through the shots, particularly in CD, towards a lower primary null. This was ignored in the modelling.

  As can be seen from figures 2(*c*) and (*d*), the magnetic profiles are similar in the two configurations until the point where the CD strikes the target while the SXD sweeps out to

---

[9] The IRVB field of view covers only the lower half of the machine, so up-down symmetry has been assumed to calculate the radiation inside the simulation grids in figures 1(*e*) and (*f*).

[10] In some of the SXD shots, transient target loading is also observed due to sawtooth MHD events in the core, for example as shown in figure 1(*h*). Such transient events were removed from the analysis window, indicated by the broken magenta line in that same figure.

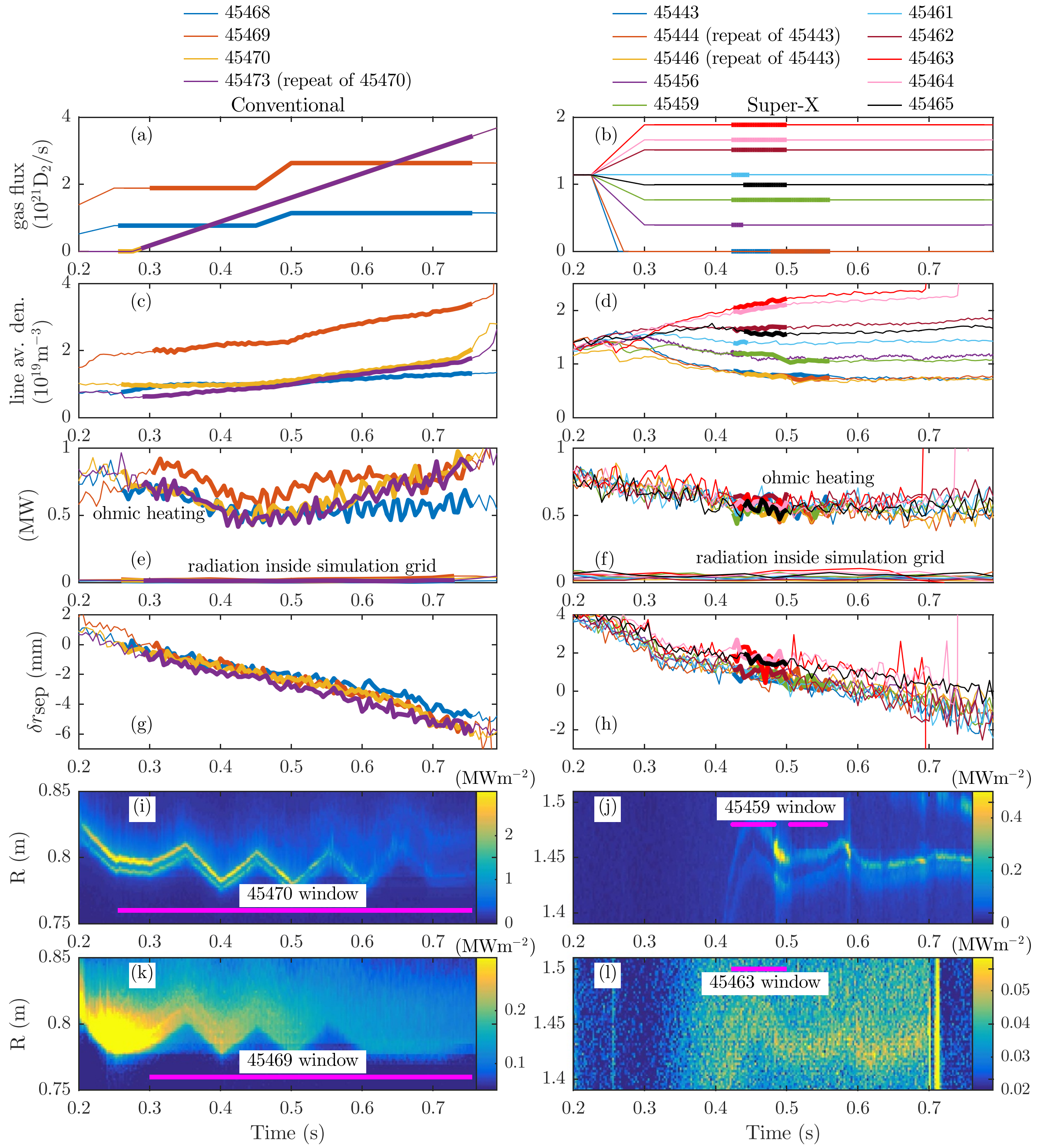

Figure 1. Overview of some important experimental time traces in CD (left column) and SXD (right column) configurations. See text and figure labels for details. Figures (*i*)–(*l*) show the infra-red target heat load as a function of time and major radius, for four example shots, demonstrating a clear strike point splitting for the lower density shots (*i*), (*j*), which is absent for the higher density shots (*k*), (*l*).

a major radius where the total magnetic field strength is 1.9 times weaker. The resulting connection length from OMP to target, $L_{\parallel}$, has been plot for CD and SXD in figure 2(*e*), as a function of $R - R_{\mathrm{sep}}$ at the OMP.

The radial extent of the CD grid on the low field side (LFS) SOL is limited by the baffle nose. By contrast, the radial extent of the SXD grid is limited by an additional null point inside the divertor volume (as indicated by the magenta asterisk in figure 2(*b*), which sits inside the baffle nose in flux space. As a result, for the structured-grid version of the code used here, the LFS SOL of the SXD grid is necessarily narrower than the LFS SOL of the CD grid. We will discuss the implications of this further in section 5.3.

- At the core boundary of the numerical grid, the net deuterium and carbon particle flux was set to zero (neutrals crossing this boundary were returned as ions), and the radial gradient of the parallel momentum was set to zero. The power crossing the core boundary was set to 0.6 MW (split

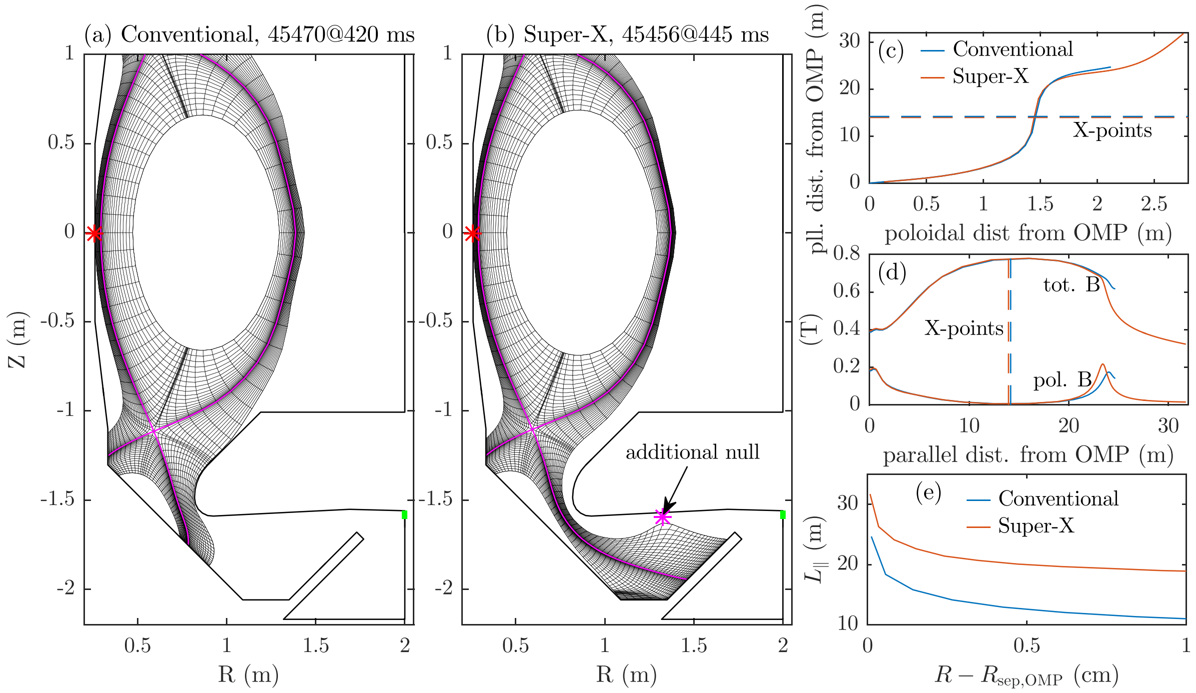

Figure 2. Simulation grids for (*a*) the CD and (*b*) the SXD configurations. Grids are up-down symmetric about $Z = 0$. Red asterisks denote the D_2 fuelling location. Small green lines denote the pumping surfaces representing the turbopumps (see text for details). The magenta line traces the separatrix. The location of the grid width-limiting null point in the SXD divertor is given by a magenta asterisk in figure (*b*). (*c*), (*d*) Plots along the first SOL flux ring of (*c*) the relationship between parallel and poloidal distance, (*d*) the total an poloidal magnetic field strength. X-points for both configurations are indicated with dashed lines. (*e*) The connection length from OMP to target, as a function of $R - R_{\mathrm{sep}}$ at the OMP, for the two configurations.

equally between electrons and ions). This value was based on the calculated ohmic heating for the experiments, shown in figures 1(*e*) and (*f*)[11].

- At the far SOL and PFR boundaries of the grid, the radial particle, electron heat and ion heat flux densities were set to factors 10^{-2}, 10^{-4} and 2×10^{-2}, respectively, of the convective fluxes associated with the local sound speed (the 'leakage' boundary condition). In addition, (as for the core boundary), the radial gradient of the parallel momentum was set to zero.
- At the sheath, boundary conditions described in section 2.5 of [19] were applied, with the secondary electron emission coefficient set to zero (no target bias potential was applied).
- Except in the upper and lower outer PFRs, the anomalous diffusive transport coefficients were set to be the same as those previously used to obtain a good match between SOLPS and a MAST L-mode plasma [24]. The anomalous particle diffusivity was set to $D_{\mathrm{AN}} = 4\ \mathrm{m^2\,s^{-1}}$ everywhere; the anomalous heat conductivities for both electrons and ions were set to $\chi_{\mathrm{AN}} = 10\ \mathrm{m^2\,s^{-1}}$ inside the separatrix and $\chi_{\mathrm{AN}} = 4\ \mathrm{m^2\,s^{-1}}$ everywhere else; the anomalous viscosity was set to $\nu_{\mathrm{AN}} = 2\ \mathrm{m^2\,s^{-1}}$ everywhere; no anomalous pinches were applied. No poloidal variation in the anomalous transport coefficients was applied[12] and the same coefficients were set for carbon ions. The exception to the above values was in the upper and lower outer PFRs, where the anomalous transport coefficients were reduced by a factor 20 compared to the SOL and inner PFR values. This was done in order to better match the experimentally observed J_{sat} profile, as shown in appendix B (figure B1). The choice to keep the anomalous transport the same throughout the scans in fuelling and divertor configuration was made deliberately to simplify the interpretation of our results, but in fact resulted in a density dependence of the SOL heat flux width approximately in line with previously-reported dependencies on MAST (see section 5.1).
- As in experiment, all plasma facing components were carbon. The surface reflection models were taken from the TRIM database [27, 28] for deuterium on carbon and carbon on carbon. For physical and chemical sputtering of carbon, the revised Bogdansky formula [29] and the flux dependent formula given in [30] were used, respectively. To mimic the fact that target and wall surfaces are not saturated with deuterium in experiment, a percentage $A_{\mathrm{wall}} =$

---

[11] On the same axes, the total radiation measured inside the respective simulation grids (according to the IRVB diagnostic, assuming up-down symmetry) is also plotted. These values suggest that the radiation inside the simulation grids was negligible.

[12] Note that a factor ~5 more power still came through the outer separatrix in the simulations due to the increased surface area and decreased flux surface spacing on the LFS. Typical factors observed on MAST for connected double null L-mode ranged between ~10 and ~20 [25, 26], but the resulting difference in power to the outer divertors (where most of this paper is focussed) would be small with these more realistic fractions.

(a) Conventional

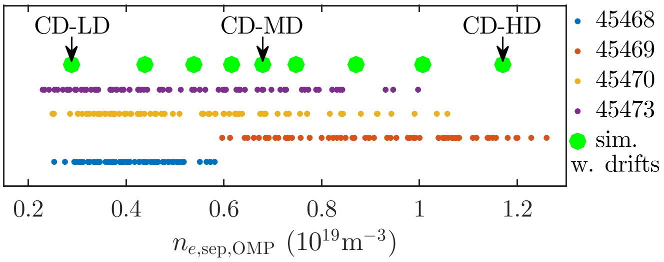

(b) Super-X

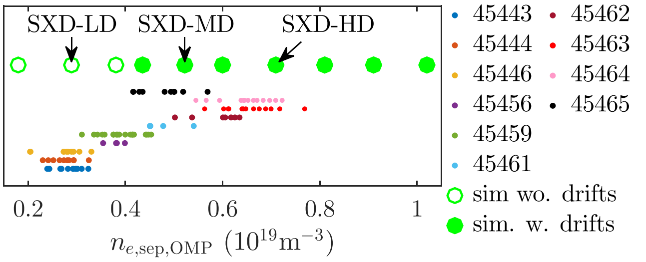

Figure 3. The range of $n_{e,\text{sep,OMP}}$ covered in experiment (coloured dots; measured with mid-plane Thomson scattering) and simulation (large green circles; open for cases without drifts, filled for cases with drifts), in (*a*) CD and (*b*) SXD configurations. Also labelled are the simulations selected for profile comparisons.

0.1% of all deuterium and carbon particles (ions, atoms and molecules) incident on target and wall surfaces were absorbed[13]. This value was kept fixed over all fuelling scans, and was chosen so that the required fuelling rate to achieve a given upstream density was approximately matched to experiment (see section 4.2).

- Parallel flux limiters were applied to account for kinetic effects at collisionalities below the formal validity range of the fluid equations, using the 'harmonic average' form described in [32]. As in [24], these were set to $\alpha_{\chi e} = 0.3$ and $\alpha_{\chi i} = 1.0$ for the electron and ion parallel heat flux, respectively, and to $\alpha_{\eta i} = 0.5$ for the ion parallel viscous flux. These values are identical to those used in the SOLPS-ITER modelling of ITER [33] (with the exception that $\alpha_{\chi i} = 0.6$ was chosen for ITER)[14].

Simulated fuelling scans were performed in CD and SXD configurations, resulting in a set of converged simulations at each fuelling rate (9 in CD and 10 in SXD; see appendix A for a catalog of all the simulations presented in this paper). The OMP separatrix electron density $n_{e,\text{sep,OMP}}$ for the default set is shown in figure 3, as large green circles. To calculate the experimental $n_{e,\text{sep,OMP}}$ values, the EFIT-derived separatrix position was shifted radially such that the simulated and experimental $n_{e,\text{sep,OMP}}(T_{e,\text{sep,OMP}})$ aligned (see section 4.1). Simulations with drifts were numerically unstable in the SXD configuration at low density, so the first three simulations in the default SXD fuelling scan were run without drifts, as indicated by the large open circles in figure 3(*b*) (drifts were turned on in all the other default simulations). For comparison to the experimental profiles in section 4, individual low density (LD), mid density (MD) and high density (HD) simulations have been picked out and labelled. Note that the low density CD (CD-LD) and the low density SXD (SXD-LD) cases have comparable $n_{e,\text{sep,OMP}}$, as do the mid density CD (CD-MD) and the high density SXD cases.

4. Experimental and simulation results

4.1. Outer mid-plane separatrix n_e and T_e

Figures 4(*a*) and (*b*) compare the experimental and simulated $n_{e,\text{sep,OMP}}$ (a) and $T_{e,\text{sep,OMP}}$ (b), as a function of an 'edge' electron density, defined here as the value averaged over -7 cm$< R - R_{\text{sep,OMP}} < -4$ cm[15]. The dots show the values measured by Thomson scattering at a location 0.5 cm radially inward from the separatrix location derived by the equilibrium reconstruction code EFIT++[37]. This shift provides a good match to the simulated $T_{e,\text{sep,OMP}}$ at lowest density, as shown in figure 4(*b*). We draw the following observations from the dots and solid lines in figures 4(*a*) and (*b*):

- After the 0.5 cm inward shift is applied, the EFIT-derived separatrix quantities have a reasonable level of agreement with the simulated values, in both configurations.
- There is a substantial (factor $\gtrsim$3) reduction in the simulated and measured $T_{e,\text{sep,OMP}}$ with increasing edge electron density. As discussed in detail in section 5.1, this reduction with $n_{e,\text{sep,OMP}}$ is larger than expected from simple two-point model estimates and is due to a combination of a transition to the sheath limited regime and stronger heat flux limiting at lower $n_{e,\text{sep,OMP}}$, along with increased convective transport (both radial and parallel) at higher $n_{e,\text{sep,OMP}}$[16].
- There is no discernible difference in $n_{e,\text{sep,OMP}}$ or $T_{e,\text{sep,OMP}}$ between CD and SXD configurations. This is consistent with the factor 1.3 increase in $L_{||}$ in SXD, implying only a factor $1.3^{2/7} = 1.08$ increase in $T_{e,\text{sep,OMP}}$.

In figure 4(*c*), we plot the resulting relationship between $n_{e,\text{sep,OMP}}$ and $T_{e,\text{sep,OMP}}$. Again, the general trend of a strongly

---

[13] In addition, to mimic the divertor turbopumps (which have a combined pumping speed of ≈10.7 m^{-3}s^{-1} [31]), 2.9% of the deuterium and carbon incident on the green surfaces in figure 2 were absorbed. Because of their much smaller surface area, however, the dominant pumping was from the target and wall surfaces.

[14] The chosen $\alpha_{\chi e} = 0.3$ is the mean of the values of 0.15 and 0.45 reported in [34] and [32], respectively, which matched bounded kinetic simulations. $\alpha_{\chi i} = 1.0$ lies between the value of 0.6 chosen for ITER simulations (based on work reported in [35]) and the value of 1.5 suggested in [32]. $\alpha_{\eta i} = 0.5$ corresponds to the value suggested in [36] and is close to the value of 4/7 calculated using Grad's 21-moment approach [32].

[15] The exact location is not important to our argument here. -7 cm$< R - R_{\text{sep,OMP}} < -4$ cm was chosen because: (i) noise is reduced by averaging over ∼3 Thomson scattering points in a region where the signal to noise ratio is relatively high compared to the separatrix region; (ii) the range lies inside the simulation grid so allows for a comparison to the simulations.

[16] We note that, as $n_{e,\text{sep,OMP}}$ increases, reduced energy fluxes crossing the first simulated flux surface could potentially also act to reduce $T_{e,\text{sep,OMP}}$. However, figures 1(*e*) and (*f*) show no evidence of that. Error field penetration may also impact the measured $T_{e,\text{sep,OMP}}$; this is not accounted for in the simulations.

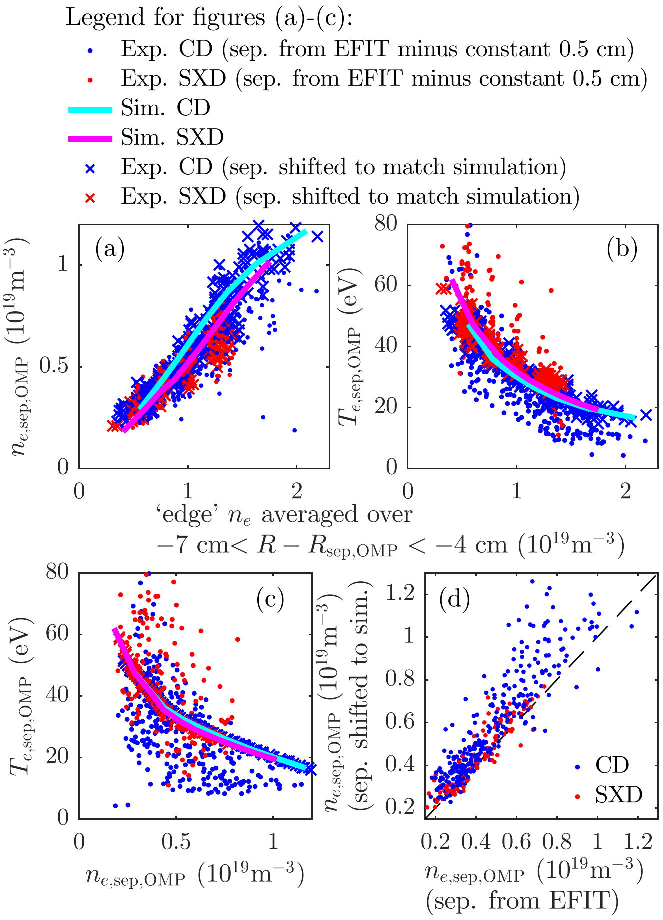

Figure 4. (*a*)–(*c*) Comparison between the outer mid-plane separatrix n_e, T_e values in experiment (dots) and simulation (solid lines), in CD configuration (blue) and SXD configuration (red). (*d*) Relationship between the experimental n_e at the location of the EFIT separatrix and the experimental n_e at the separatrix after an unrestricted shift to the profiles in order to match the simulated trend of $T_{e,\mathrm{sep,OMP}}(n_{e,\mathrm{sep,OMP}})$. The latter are the experimental $n_{e,\mathrm{sep,OMP}}$ used in the rest of this paper, unless otherwise stated. See text for details.

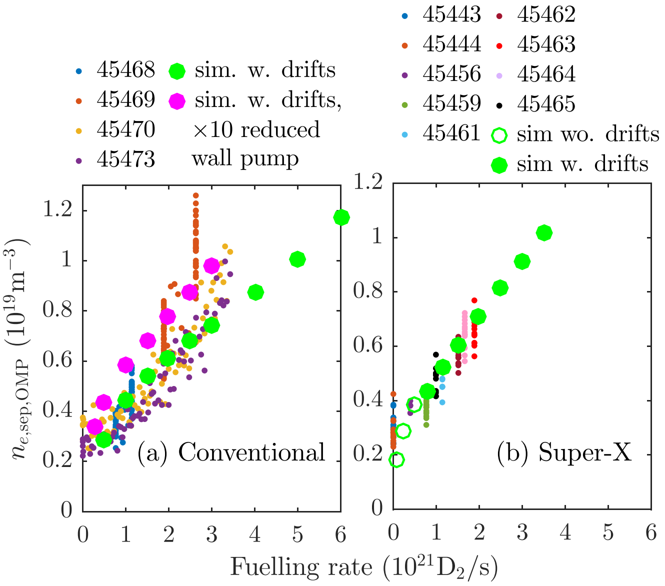

Figure 5. Comparison of the variation in $n_{e,\mathrm{sep,OMP}}$ as a function of the inner mid-plane fuelling rate, in experiment (small coloured dots), in the default simulations (large green circles), and in (*a*) CD and (*b*) SXD configurations. For CD, simulations with a factor 10 reduction in the wall pumping are also shown as large magenta circles.

decreasing $T_{e,\mathrm{sep,OMP}}$ with increasing $n_{e,\mathrm{sep,OMP}}$ is observed, although there is a significant level of noise in the experimentally measured values. This noise comes from a combination of the Thomson scattering diagnostic itself, the EFIT reconstruction, and/or plasma turbulence. In order to reduce the noise in the measured $n_{e,\mathrm{sep,OMP}}$ that we will use in the rest of this paper, we have applied an unrestricted shift in each measured Thomson profile, such that the simulated trend of $T_{e,\mathrm{sep,OMP}}(n_{e,\mathrm{sep,OMP}})$ is recovered. These shifted separatrix values are shown in figures 4(*a*)–(*c*) as crosses (by definition, they lie directly underneath the simulated data in figure 4(*c*).

Our assumption by making this unrestricted shift is that deviations from the simulated trend of $T_{e,\mathrm{sep,OMP}}(n_{e,\mathrm{sep,OMP}})$ are dominated by measurement noise rather than physics differences between code and experiment. This methodology is useful in terms of reducing the noise on $n_{e,\mathrm{sep,OMP}}$, but has the drawback that differences between the simulated and experimental $T_{e,\mathrm{sep,OMP}}(n_{e,\mathrm{sep,OMP}})$ can lead to interpretation issues. In particular, a suspected separatrix pressure drop in the CD configuration experiments at highest density does not show up in the simulations (at least not stably). See section 5.4 for further discussion. Aside from this particular issue, though, the choice to shift the EFIT separatrix position to match the simulated $T_{e,\mathrm{sep,OMP}}(n_{e,\mathrm{sep,OMP}})$ does not affect our conclusions in this paper. T here is a good correlation between the experimentally-inferred $n_{e,\mathrm{sep,OMP}}$, shifted to match the simulations, and the experimentally-inferred $n_{e,\mathrm{sep,OMP}}$from EFIT without any shift (figure 4(*d*)), with a median factor 1.14 increase in the former compared to the latter. Furthermore, the median required shift to match the simulations exactly was -0.64 cm, well within the expected uncertainty in the EFIT separatrix position.

4.2. Fuelling rates

Figure 5 shows the experimental and simulated $n_{e,\mathrm{sep,OMP}}$ as a function of the D_2 fuelling rates in (a) CD and (b) SXD configuration. The experimental fuelling rates are instantaneous values within the analysis time windows for each shot (bold lines in figures 1(*a*) and (*b*)), whilst each simulation value is an input to a steady-state simulation within a fuelling scan.

The experimental relationship between fuelling rate and $n_{e,\mathrm{sep,OMP}}$ was approximately linear and agrees tolerably well with the simulations. The behaviour was similar in both configurations ($\mathrm{d}n_{e,\mathrm{sep,OMP}}/\mathrm{d}$(fuelling rate)$\sim 0.16 \times 10^{-3}$ (el./m^3)/(D$_2$/s) in CD simulations vs $\sim 0.22 \times 10^{-3}$ (el./m^3)/(D$_2$/s) in SXD simulations). In the simulations, this relationship was only weakly dependent on the wall pumping fraction; a factor 10 reduction in the wall (including targets) pump fraction (from $A_{\mathrm{pump}} = 0.1\%$ by default, to $A_{\mathrm{pump}} = 0.01\%$) resulted in a relatively small ($\sim$25%–50%) increase

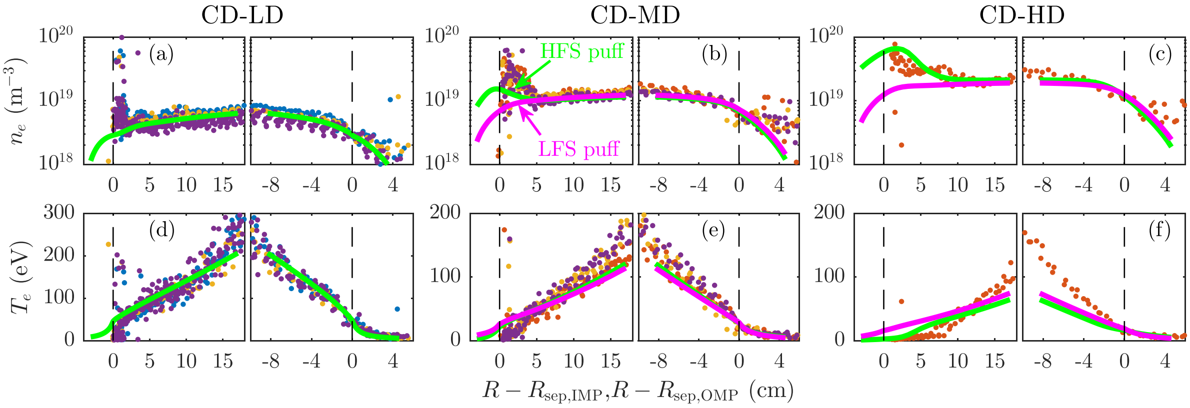

Figure 6. Mid-plane electron density (*a*)–(*c*) and temperature (*d*)–(*f*) profiles in simulation and experiment (from Thomson scattering measurements), in the CD configuration. Low, mid and high density simulations are selected as labelled in figure 3(*a*). The same colour coding for the different shots is used as in figure 1. Green lines show the default simulation set with fuelling at the high field side, magenta lines show equivalent simulations with the fuelling moved to the low field side.

in the simulated $n_{e,\mathrm{sep,OMP}}$ for a given fuelling rate (magenta circles in figure 5(*a*). We conclude that the choice of $A_{\mathrm{pump}} = 0.1\%$ was acceptable for our purposes.

4.3. Mid-plane profiles

Figure 6 shows (*a*)–(*c*) the mid-plane n_e and (*d*)–(*f*) the mid-plane T_e profiles in simulation and experiment, for the CD configuration. The three columns in the figure show comparisons for the low (CD-LD), mid (CD-MD), and high (CD-HD) density simulations, as labelled in figure 3(*a*). For each of these three simulations, experimental profiles that were within the analysis time window and whose $n_{e,\mathrm{sep,OMP}}$ value was within 2×10^{17} m^{-3} of the simulation, were selected for comparison. These experimental profiles were measured by the Thomson scattering system, which collects data across the full radial span of the mid-plane plasma [38]. Profiles are plotted as a function of the major radius relative to either the inner or the OMP separatrix position[17]. Different colours represent different shots, with the same colour coding as in figure 1.

The agreement along the OMP is reasonable throughout the scan, especially given that, for all simulations, the anomalous transport coefficients in the core and SOL were kept the same as for previously fitted MAST L-mode simulations. This implies similar radial transport between MAST and MAST-U, at least for these L-mode plasmas. Of particular interest are the inner mid-plane density profiles, which exhibit peaking in the density near the separatrix and are consistent with previous observations on MAST [39]. In the simulations, this peaking is due to local ionisation of neutrals from the HFS puff (red asterisks in figures 2(*a*) and (*b*)). This can be inferred by comparison to the magenta profiles, for which the simulated puff location was moved to the LFS and for which no density peaking was observed. In similar experiments with LFS fuelling, we note that no density peaking was discernible either (data not shown), suggesting that the same mechanism is also responsible in experiment.

For HFS gas fuelling at high density, the simulated electron temperature at the inner mid-plane separatrix becomes particularly low relative to the OMP value ($T_{e,\mathrm{sep,IMP}} = 2.6$ eV vs. $T_{e,\mathrm{sep,OMP}} = 16.5$ eV for the green lines, representing the simulation values, in figure 6(*f*). A strong drop is also apparent in the experiment. This cooling appears to be driven by the HFS puff, as demonstrated by the equivalent LFS fuelled simulation, for which the inner and OMP separatrix T_e values remain similar at the same density ($T_{e,\mathrm{sep,IMP}} = 15.8$ eV vs. $T_{e,\mathrm{sep,OMP}} = 19.0$ eV for the magenta lines in figure 6). This is consistent with the observation that the eventual radiative collapse in the simulations occurs at higher density for the LFS fuelled simulations, as discussed further in section 5.4 (figure 18).

Figure 7 shows the same mid-plane comparisons for the SXD configuration. As in the CD configuration, the agreement with the Thomson scattering profiles is reasonable throughout the fuelling scan. Note that the HFS density peaking is less pronounced in SXD because the maximum HFS fuelling rate achieved experimentally was lower compared to the CD configuration.

4.4. Target ion fluxes

For the discharges of interest, Langmuir probe ion flux data was available from the upper and lower outer targets. Data was available from toroidal sector 4 (of 12 evenly distributed sectors) for the upper outer target in CD, from sectors 4 and 10 for the upper outer target in SXD, and from toroidal sector 10 for the lower outer target in both CD and SXD.

Detailed comparisons of the experimental and simulated target profiles (which justify the reduced anomalous transport in the outer PFR applied to the default simulations) are provided in appendix B. Here, we focus on the variation of target ion flux with upstream density. Figure 8 shows (*a*) the

---

[17] For the inner mid-plane separatrix position, the EFIT-derived separatrix position was used (without any shift). This resulted in an apparent offset of ∼2 cm between the experimental and simulation profiles on the inboard side, but no attempt was made to rectify this. For the OMP separatrix position (as mentioned in section 4.1) a shift was introduced in order to match the simulated ($T_{e,\mathrm{sep,OMP}}, n_{e,\mathrm{sep,OMP}}$) values.

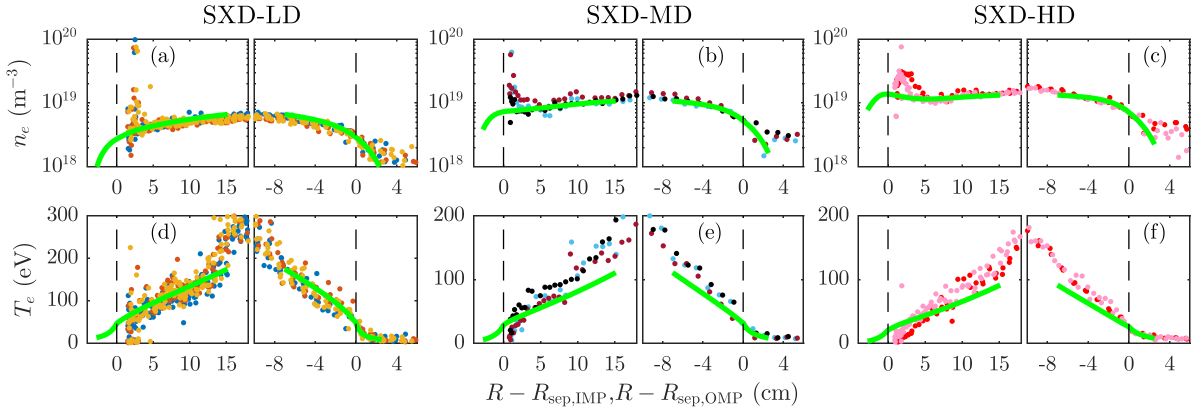

Figure 7. Mid-plane electron density (*a*)–(*c*) and temperature (*d*)–(*f*) profiles in simulation and experiment (from Thomson scattering measurements), in the SXD configuration. As figure 6 but for the SXD.

near separatrix[18] ion particle flux density normal to a toroidally flat target surface[19], $\Gamma_{\perp t}$, and (*b*) the integrated $\Gamma_{\perp t}$ to the outer targets as a function of $n_{e,\rm sep,OMP}$. Results are shown in experiment and simulation, for CD and SXD configurations, as labelled. The reader is advised of the large uncertainties associated with the faded markers, which represent shots with strike point splitting.

Consider first the near separatrix $\Gamma_{\perp t}$ shown in figure 8(*a*). The simulations broadly fall close to the spread in the experimental data. The exception is the CD upper outer target, which exhibits a steeper decrease after rollover in experiment (blue dots) than simulation (blue solid line); the simulation values do roll over, but only weakly at both targets. A similar discrepancy is seen in the integrated $\Gamma_{\perp t}$ to the CD upper outer target (figure 8(*b*)); the experimental flux drops by $\gtrsim 50\%$ whilst the simulation fails to rollover at all. Note that, at the *lower* outer target in CD (blue open circles), there is no decrease in the measured near separatrix $\Gamma_{\perp t}$. In fact the value *increases* slightly with increasing $n_{e,\rm sep,OMP}$. Equivalent integrated measurements at the lower outer target were not available in CD (no open circles in figure 8(*b*)) due to gaps in probe coverage.

In SXD, the integrated $\Gamma_{\perp t}$ is higher in the simulations than experiment within the narrow density range where strike point splitting was absent. As shown in section 5.3, the small drop that does occur in SXD after rollover can be largely attributed to particles leaving the side of the relatively narrow SXD numerical grid. This suggests that the discrepancy on a wider grid would be even larger (note that we do not expect a wider grid to influence the near separatrix $\Gamma_{\perp t}$ trend shown in figure 8(*a*). It should be noted, however, that there is also a significant discrepancy within the experimental data iteself, between opposite toroidal sectors (red dots vs red asterisks in figure 8(*b*))[20].

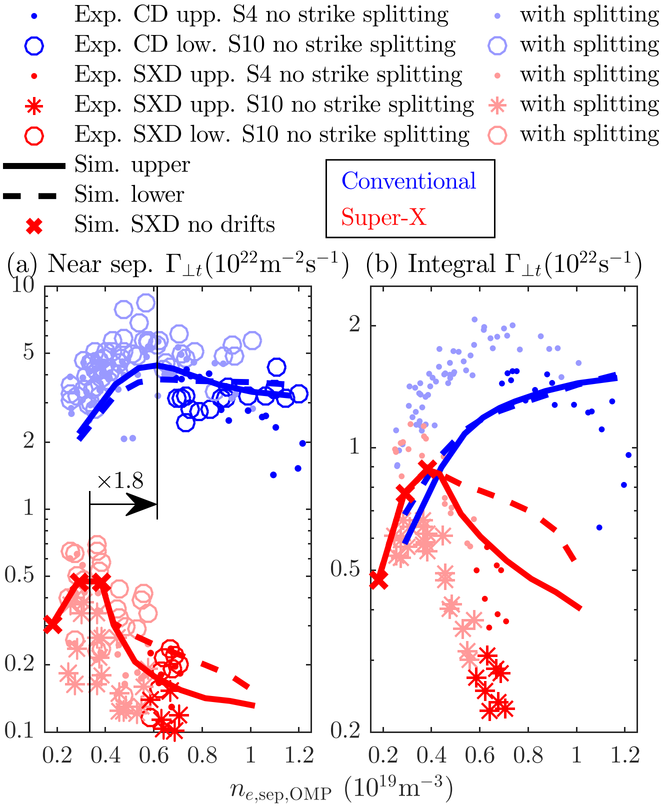

Figure 8. (*a*) Near separatrix and (*b*) integrated $\Gamma_{\perp t}$ to the outer targets, as a function of $n_{e,\rm sep,OMP}$. CD and SXD data are shown in blue and red, respectively. Markers and lines represent experimental and simulation data, respectively, as described in the legend. Shots with strike point splitting are plotted in faded colours, to emphasise uncertainty.

There are several possible reasons for the discrepancy between simulations and experiment which, in reality, may be

---

[18] This 'near separatrix' $\Gamma_{\perp t}$ is averaged over a region $0 \leqslant R - R_{\rm sep,OMP} \leqslant$ 2.5 mm (mapped back to the mid-plane), typically at least a factor 5 narrower than the fall off length in $\Gamma_{\perp t}$.

[19] In reality, the divertor tiles are tilted toroidally. Using the EFIT equilibrium reconstruction, as well as the probe collection area and tilt, we have post-calculated this $\Gamma_{\perp t}$ to allow comparison to the toroidally symmetric SOLPS-ITER results.

[20] This may be attributed, at least in part, to the differing probe design at the two toroidal locations [40], offering different collection areas. A quantitative explanation for the observed discrepancy is still under investigation.

acting in combination. Firstly, in CD, there is a reduction in δr_{sep} through the analysis windows (figure 1(*i*)), with the equilibrium shifting slightly towards a lower primary null as the density increases. This is consistent with the upper outer near separatrix $\Gamma_{\perp t}$ dropping while the lower outer value increases (in the density range 0.7×10^{19} m$^{-3} \gtrsim n_{e,\mathrm{sep,OMP}} \lesssim 1.2 \times 10^{19}$ m^{-3}), whilst the simulated values (which assume $\delta r_{\mathrm{sep}} = 0$ throughout) stay approximately constant. Secondly, the experimental rollover in CD may in part be attributed to an unstable collapse in the core radiation due to neutrals puffed from the HFS; the steady state simulations do not capture this collapse. This possibility is discussed further in section 5.4. Finally, in both CD and SXD, there may be important neutral physics missing or incorrect in the simulations. In particular, we note that the default neutral model (used here) likely underestimates the conversion of D_2 to D_2^+, and therefore also the reduction in target flux due to molecular activated recombination (MAR) [41–43].

As noted above, the simulated rollover in the near separatrix $\Gamma_{\perp t}$ is weak in the CD configuration. Furthermore, to resolve the rollover in SXD, it was necessary to turn drifts off at the lower fuelling rates, to avoid numerical instabilities at the hot upper inner target. Nevertheless, it is worth noting (as indicated in figure 8(*a*)) that rollover in the CD occurs at a value of $n_{e,\mathrm{sep,OMP}}$ that is 1.8 times greater than in the SXD. Simple arguments [13, 15] based either on modified[21] two-point model calculations of the target temperature [44], or the conditions required for radiation of all the plasma power [8], predict this factor to be given by $(B_\times/B_t)_{\mathrm{SXD}}/(B_\times/B_t)_{\mathrm{CD}}$, where $B_\times$ and B_t are the magnetic field strengths at the X-point and target, respectively (figure 2(*d*)). This gives a predicted factor of 1.9, close to the value observed in the simulations. Due to the strike point splitting, a similar factor cannot be given in experiment, strongly motivating the pursuit of similar experiments without strike point splitting in future.

4.5. Target heat loads

Infra-red camera measurements were made at the lower outer target, and surface heat loads $Q_{\perp t}$ were inferred using the methodology described in [26], with a surface layer coefficient of $\alpha = 200$ kWm^{-2}K^{-1}[22]. The tile emissivity ϵ used for this calculation was based on lab measurements of tiles equivalent to those in vessel. Above a surface temperature of $T_{\mathrm{surf}} \gtrsim 40$ °C, the emissivity of both CD and SXD tiles was found to saturate at $\epsilon \approx 0.8$. For $T_{\mathrm{surf}} \lesssim 40$ °C, a strong reduction in ϵ was observed for the CD tiles, but data was not available at these temperatures for the SXD tiles. Since $T_{\mathrm{surf}} \lesssim 40$ °C is relevant for the SXD shots analysed here, this leads to uncertainties in the exact emissivities for the SXD target, which are represented by the red error bars in figures 9(*a*) and (*b*)[23]. Further uncertainties arise, particularly for the SXD, due to corruption by volumetric radiation inside the IR camera's frequency band (tending to overestimate the loads) as well as low signal-to-noise levels. Neither of these are accounted for in the red error bars, however. Nor do the error bars reflect uncertainties due to strike point splitting. For both CD and SXD, an approximately constant background noise heat load profile was calculated from a time average over periods at the start and end of the shot when there was no plasma present, and subtracted from the derived profile (this background noise level was ~0.025 MWm^{-2} in CD and ~0.013 MWm^{-2} in SXD).

Figure 9 demonstrates the impact of the SXD configuration on the heat loads to the lower outer target. In figure 9(*a*), the peak $Q_{\perp t}$ is plotted as a function of $n_{e,\mathrm{sep,OMP}}$, in CD (blue) and SXD (red) configurations, in experiment (dots for CD, error bars for SXD) and simulation (solid lines), as labelled. Shots with strike point splitting are again shown in faded colours. The main components of the simulated peak heat loads are also given, due to the kinetic energy of plasma particles (dashed lines), the potential energy released when ions and electrons recombine in the target substrate (dotted lines), and the kinetic energy of the neutral particles (dash-dotted lines)[24]. In both configurations, as $n_{e,\mathrm{sep,OMP}}$ increases, the simulated surface recombination load becomes increasingly important relative to the plasma kinetic load, but it is only in the SXD configuration that the surface recombination load also drops to be comparable with the neutral kinetic load.

It is important to realise that, although (as discussed in the previous section) the strike point splitting at low density hampers an experimental inference of the difference in $n_{e,\mathrm{sep,OMP}}$ required for rollover in CD vs. SXD, there *does* exist a narrow window in which the CD and SXD $n_{e,\mathrm{sep,OMP}}$ values overlap in the absence of strike point splitting (non-faded blue dots and red error bars in figure 9(*a*). Figure 9(*b*) compares the target heat load profiles for CD and SXD shots within that window. As indicated by the horizontal arrows, the experimental data is taken within the vertical black lines in figure 9(*a*). These fall within $\pm 10^{17}$ m^{-3} of the $n_{e,\mathrm{sep,OMP}}$ values for the CD-MD ($n_{e,\mathrm{sep,OMP}} = 0.68 \times 10^{19}$ m^{-3}) and SXD-HD ($n_{e,\mathrm{sep,OMP}} = 0.71 \times 10^{19}$ m^{-3}) simulations, i.e. at comparably similar $n_{e,\mathrm{sep,OMP}}$. Importantly, as seen in figure 9(*c*), the OMP n_e and T_e profiles are similar at these comparable values of $n_{e,\mathrm{sep,OMP}}$. Furthermore, the SXD simulation exhibits a factor 26.8 reduction in peak heat load compared to the CD simulation. This reduction is due to a combination of a more exhaust-favourable geometry and increased dissipation in the SXD, as follows.

---

[21] Modified to account for a varying magnetic field stength along SOL field lines.

[22] This value of surface layer is sufficient to effectively ignore surface layer effects.

[23] The lower value corresponds to $\epsilon = 0.7$ and the upper value to $\epsilon = f(T_{\mathrm{surf}})$, where f is the measured functional form for the CD tiles. This reflects our uncertainty as to whether the same reduction in ϵ for $T_{\mathrm{surf}} \gtrsim 40$ °C occurs for the SXD tiles as measured for the CD tiles.

[24] The loads due to radiation and due to atoms combining into molecules in the target substrate were found to be negligible and are not shown.

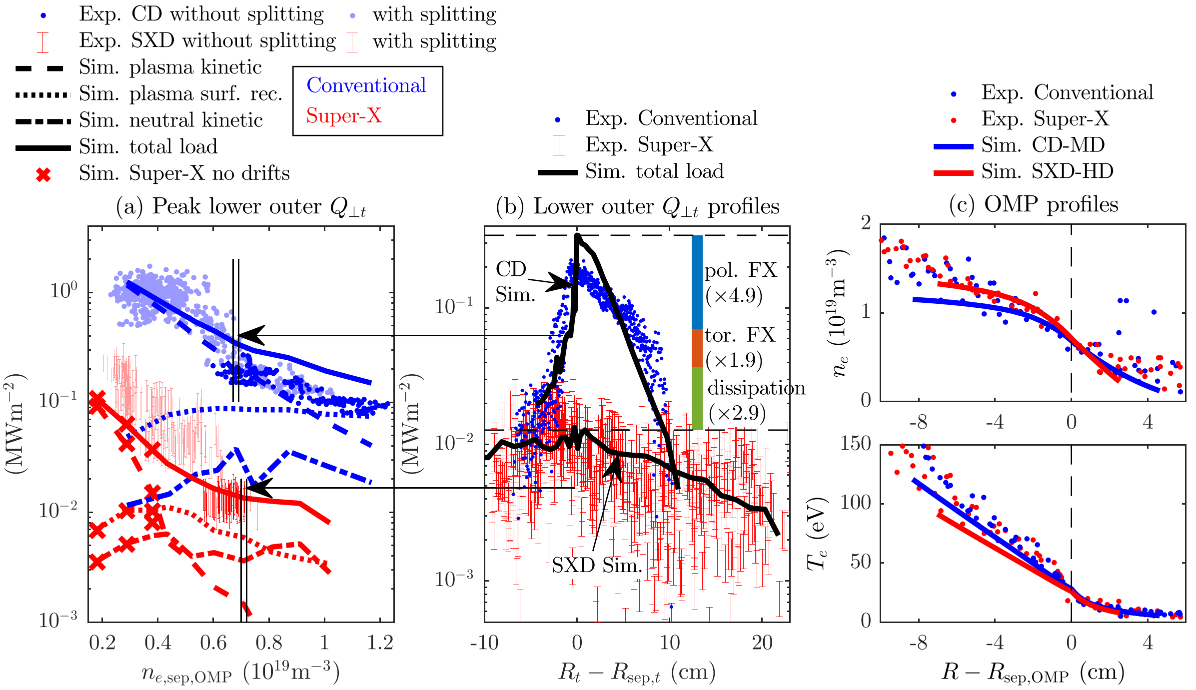

Figure 9. The impact of the SXD configuration on heat loads to the lower outer target. (*a*) The peak heat load as a function of $n_{e,\mathrm{sep,OMP}}$, in CD and SXD, in simulation and experiment. Simulation components are also shown, as labelled. (*b*) Heat load profiles as a function of major radial distance past the separatrix. CD-MD and SXD-HD simulations are shown, which have similar values of $n_{e,\mathrm{sep,OMP}}$. Experimental data is taken from within the black vertical bars in figure (*a*). The coloured vertical bar in (*b*) shows the factor drops in the simulated peak $Q_{\perp t}$, from CD to SXD, resulting from poloidal flux expansion, toroidal flux expansion, and additional SXD dissipation. (*c*) The OMP profiles of n_e (top) and T_e (bottom) for the same CD-MD and SXD-HD simulations. This is the same data previously presented in figures 6(*b*), (*e*) and 7(*c*), (*f*), brought together to demonstrate the similar upstream profiles in the two configurations.

The expected factor reduction in heat load due to geometry alone is given by [14, 45]

$$\left(\frac{Q_{\perp t\mathrm{CD}}}{Q_{\perp t\mathrm{SXD}}}\right)_{\mathrm{geom}} = \frac{\mathrm{FX}_{\theta\mathrm{SXD}}}{\mathrm{FX}_{\theta\mathrm{CD}}}\frac{\mathrm{FX}_{\phi\mathrm{SXD}}}{\mathrm{FX}_{\phi\mathrm{CD}}}\frac{\mathrm{FX}_{\mathrm{tilt,SXD}}}{\mathrm{FX}_{\mathrm{tilt,CD}}}, \quad (1)$$

where

$$\mathrm{FX}_\phi = R_t/R_u \quad (2)$$

is the toroidal flux expansion (subscript 'u' represents the value at the divertor entrance),

$$\mathrm{FX}_\theta = \frac{B_{\theta u}/B_{\phi u}}{B_{\theta t}/B_{\phi t}} \quad (3)$$

is the poloidal flux expansion (subscripts 'θ' and 'ϕ' represent poloidal and toroidal components, respectively), and

$$\mathrm{FX}_{\mathrm{tilt}} = \frac{1}{\sin(\alpha_{\mathrm{tilt}})} \quad (4)$$

is the flux expansion due to target tilting in the poloidal plane (α_{tilt} is the angle between the tilted target and the flux surface). For the equilibria used here (figure 2), the difference in α_{tilt} was deliberately kept small ($\mathrm{FX}_{\mathrm{tilt,SXD}}/\mathrm{FX}_{\mathrm{tilt,CD}} = 1.01$). The additional poloidal flux expansion in the SXD provides a factor $\mathrm{FX}_{\theta\mathrm{SXD}}/\mathrm{FX}_{\theta\mathrm{CD}} = 4.9$ reduction in the peak heat load, while the toroidal flux expansion provides a further factor $\mathrm{FX}_{\theta\mathrm{SXD}}/\mathrm{FX}_{\theta\mathrm{CD}} = 1.9$ reduction. These factors are plotted in figure 9(*b*) as vertical blue and red bars, respectively, starting from the peak heat load in the CD simulation (the logarithmic *y*-axis here means that the length of each bar is proportional to the reduction factor they represent). In total, the expected reduction due to geometry is a factor 9.3. The actual simulation reduction is a factor 26.8, implying a further factor 2.9 reduction in SXD due to increased dissipation along the flux tube. This important additional dissipation in the SXD simulation is analysed further in section 5.2.

The measured peak load reduction factor from the IR data is slightly lower than in the simulations, primarily due to an ~80% overestimate of the peak load in the CD simulation. From the natural deviation in the CD loads and the uncertainty in the SXD tile emissivity, we estimate a reduction factor between 9 and 23 in experiment. Given that the simulations (with a reduction factor of 26.8) suggest a value at the upper end of this range, and that volumetric radiation likely leads to, if anything, an overestimate of the inferred SXD heat loads in experiment, it is highly likely that the experimental reduction in peak heat load at this $n_{e,\mathrm{sep,OMP}}$ is at least the factor 9.3 expected from geometry alone, and probably a factor ~2 more due to increased dissipation in the SXD configuration.

4.6. Measurements within the SXD divertor volume

4.6.1. Dα emission. MAST-U is fitted with two independent spectroscopy diagnostics in the lower outer divertor: a multi wavelength imaging (MWI) filtered camera diagnostic

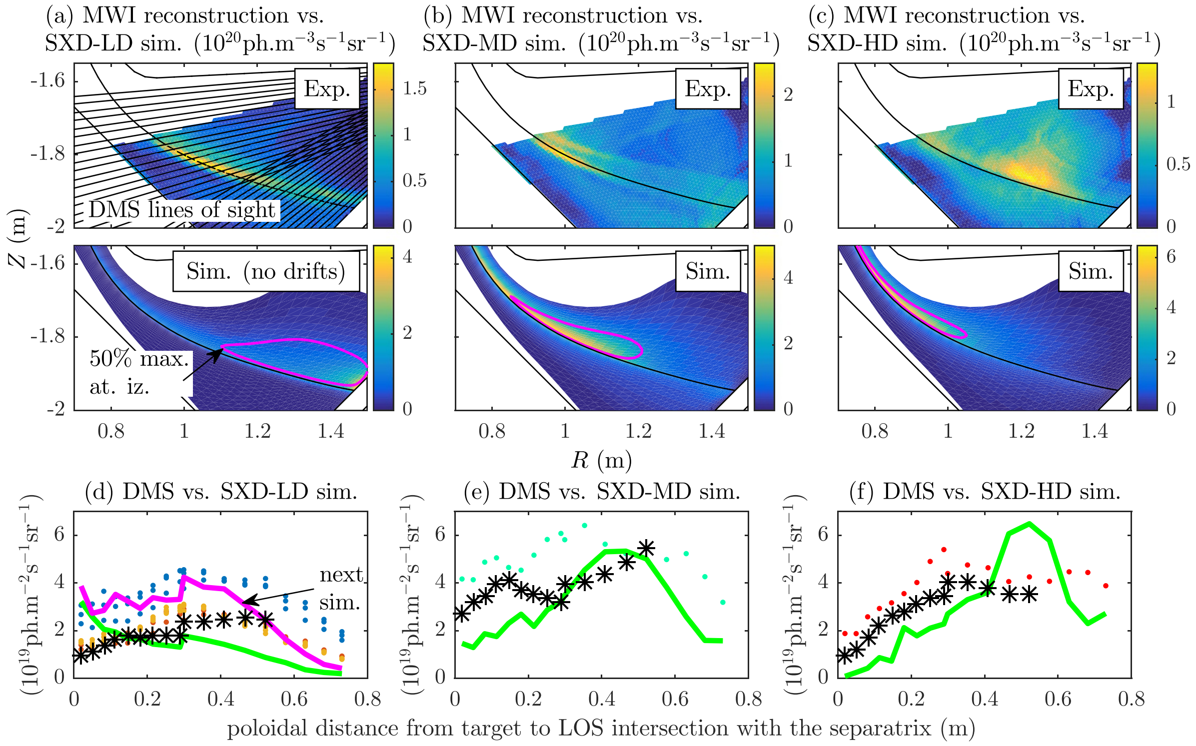

Figure 10. Comparison between the lower outer divertor Dα emissivity in simulation and experiment, in SXD configuration. (*a*)–(*c*) First row: experimental 2D poloidal Dα emissivity reconstructions from MWI, at comparable $n_{e,\mathrm{sep,OMP}}$ to the SXD-LD (*a*), SXD-MD (*b*) and SXD-HD (*c*) simulations. Second row: the simulated emissivity profiles. The simulated separatrix position is shown as a black line. (*d*)–(*e*) DMS line of sight integrals measured in experiment (dots; same colour coding by shot as in figure 1) and post-calculated from the simulations (solid green lines). The line of sight integrals through the MWI reconstructions are also shown as black asterisks. In (*d*), the simulated line of site integrals are also shown in magenta for the very next simulation in the fuelling scan.

[46, 47] and a divertor monitoring spectroscopy (DMS) line of sight diagnostic [48]. Figures 10(*a*)–(*c*) (first row) show 2D MWI reconstructions of the Dα emissivity in the poloidal plane, for experimental densities comparable to the (*a*) SXD-LD, (*b*) SXD-MD and (*c*) SXD-HD simulations. These reconstructions were sorted into bins (of width 3×10^{17} m^{-3}), according to their $n_{e,\mathrm{sep,OMP}}$, and the mean reconstruction was calculated in each bin. The post-calculated 2D Dα emissivity profiles are shown directly below the experimental reconstructions for comparison. In magenta, we have overlayed a contour at 50% of the maximum atomic ionisation.

Figures 10(*d*)–(*f*) again show a comparison to the Dα emissivity, now for the integrated line of sight values measured by the DMS diagnostic. The lines of sight are shown in figure 10(*a*) (their toroidal component is negligible). Dots in figures 10(*d*)–(*f*) show the DMS measurements, colour coded by shot as in figure 1(the same binning in $n_{e,\mathrm{sep,OMP}}$ was applied as for the MWI reconstructions). Line of sight integrated values are plotted as a function of the poloidal distance from the target to the point where that line of sight intersects the separatrix. Also shown for comparison are the line of sight integrated values for the MWI (black asterisks, calculated by integrating the reconstructions in the first row of figures 10(*a*)–(*c*) and the line of sight integrated values for the simulations (green lines, calculated by integrating the profiles in the second row of figures 10(*a*)–(*c*).

The following observations can be made of figure 10:

- In general, the consisitency between the MWI reconstructions and the independent DMS measurements is acceptable, although at mid-density (figure 10(*e*)) there is some discrepancy between the two in the middle part of the profile (see [47] for a discussion of the likely reasons for such discrepancies).
- At low density (figures 10(*a*) and (*d*)), the Dα emission is peaked at the target in the simulation, but is spread more evenly along the leg in experiment (according to MWI and DMS measurements). This implies that the simulation (without drifts at this density) is more attached than its experimental counterpart, with D atoms more able to move up the leg in experiment. Note, however, that at this density, the simulations are highly sensitive to $n_{e,\mathrm{sep,OMP}}$; the very next simulation in the fuelling scan (magenta line in figure 10(*d*), still without drifts) shows a much closer resemblence to the experimental profiles with just a 30% increased $n_{e,\mathrm{sep,OMP}}$. The disagreement may therefore be explained at least in part by uncertainties in the experimental value of $n_{e,\mathrm{sep,OMP}}$.
- At mid density, the agreement between simulation and experiment is improved. In both cases, the peak has moved off the target, but is slightly further up the leg in experiment compared to simulation. Strike point splitting in the MWI reconstruction is clearly visible and is not accounted for in

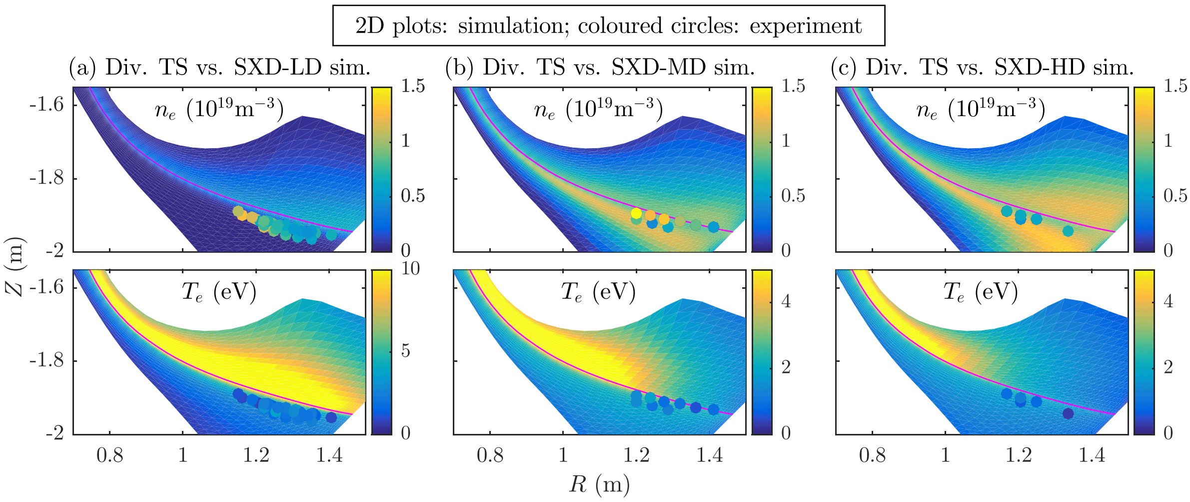

Figure 11. Comparison between the lower outer divertor n_e and T_e in simulation and experiment, in SXD configuration. Experimental measurements from divertor Thomson scattering are plotted on top of the 2D simulated profiles, for the SXD-LD (*a*), SXD-MD (*b*) and SXD-HD (*c*) simulations, for n_e (first row) and T_e (second row).

the simulation. Note that this simulation has drifts turned on, but the Dα profile is very similar without drifts.

- At the highest density, the simulation still agrees reasonably well with the DMS measurements, and with the line-of-sight-integrated MWI values. However, the 2D MWI reconstruction is different to the simulated profile; the Dα peak associated with atomic ionisation, seen in figure 10(*b*) (top), has now left the viewing region in experiment, leaving behind an emissivity profile with a large radial spread. Consistent with the analysis in [48], we hypothese this remaining emission to be driven primarily by the dissociation of D_2^+ molecular ions into n = 3 excited atoms. As can be seen in figure 10(*f*) in the near target region, this Dα emission due to molecular ions is not observed in the code, possibly due to an underestimate of the ion conversion rate used in the simulations to convert D_2 molecules into D_2^+ [42]. Related to this, in all three simulations, the peak in the simulated Dα emission correlates well with the peak in the atomic ionisation. However, due to an increased contribution to the Dα emission from dissociated D_2^+, this is not expected to be the case in experiment [48].

4.6.2. Divertor Thomson scattering. The divertor Thomson scattering diagnostic [49] was also active during this experiment. The comparison between simulations and experiment is shown in figure 11, and is in qualitative agreement with the above analysis of the Dα emission[25]. At low density, the majority of the data points lie in the PFR (a result of small movements in the separatrix position across the different shots). In this region, where radial gradients are strong, it is difficult to draw useful conclusions on the comparison between simulation and experiment due to errors in the exact separatrix position. However, at mid density, there are sufficient measurements near the separatrix to conclude a reasonable match to the simulations, given the experimental scatter. At high density, the measurement points sit in a deeply detached region, where errors in the simulated molecular rates (discussed above) will be exacerbated. Consistent with the hypothesis that the simulations are underestimating MAR in this region (recall the underestimate of the target flux reduction in figure 8(*b*) as well as the underestimate of the molecular contribution to the Dα emission in figure 10(*c*), the electron density in this deeply detached region is overestimated by the simulations.

4.6.3. Fulcher emission. Figure 12 is a repeat of figure 10, but for the normalised molecular Fulcher band emission[26]. All plots in figure 12 are normalised to their maximum value[27]. Focussing first on the qualitative changes in the emission (quantified in the next subsection), we see a picture emerge that is consistent with the Dα emission: at low density, there is considerably more Fulcher emission up the leg than in the simulation, suggesting that molecules (as well as atoms) are more able to move up the leg in experiment. Again, the agreement is much closer for the very next simulation in the fuelling scan (shown in magenta in figure 12(*d*)), suggesting a strong sensitivity to $n_{e,\mathrm{sep,OMP}}$. At mid density, the agreement between simulation and experiment is good, although the poloidal distance between the maximum and 50% Fulcher emission is increased

---

[25] A slightly wider bin width of 7×10^{17} m^{-3} was required for binning of the experimental data here, due to the reduced time resolution of the divertor Thomson scattering diagnostic.

[26] In experiment, a filter from 595 nm to 605 nm and from 592.5 nm to 612.5 nm was applied for the MWI and DMS diagnostics, respectively. In the simulations, the Fulcher band emission was post-calculated by multiplying the electron density, the D_2 molecule density and the H.12 2.2.5fl rate coefficient from the AMJUEL database [50].

[27] Except for the MWI reconstruction in figure 12(*c*), for which the maximum was deemed to have left the viewing region and the last resolved maximum was used for normalisation. See section 4.6.4 for details.

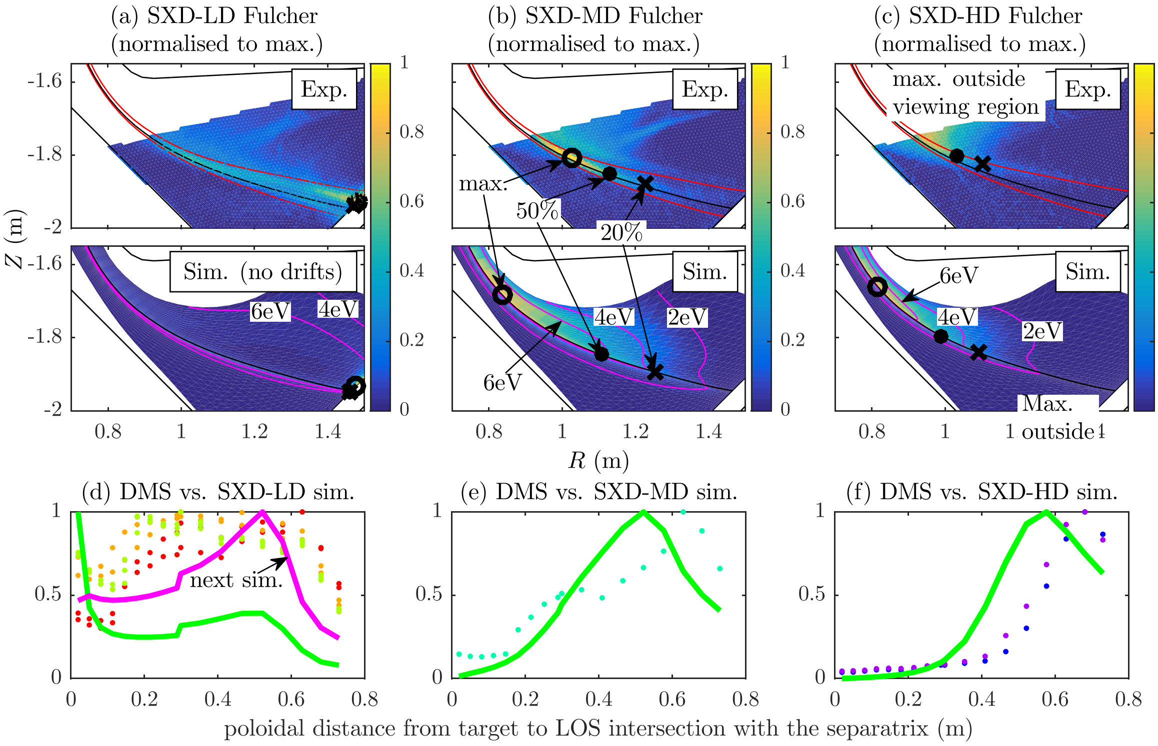

Figure 12. Repeat of figure 10, for the molecular Fulcher band emission (normalised to its maximum). The calculated positions of the 20% and 50% Fulcher fronts are shown as black crosses and filled circles, as labelled. For comparison, simulated electron temperature isotherms are also plotted in magenta, as labelled. The locations of maximum Fulcher emission are shown as open circles in (*a*) and (*b*). In (*c*), the maximum was deemed to be outside of the MWI viewing region and so the last resolved maximum was used for normalisation.

in experiment, suggesting a steeper drop in T_e than in the simulation. At high density, the location of the 50% and 20% Fulcher emission still agrees well with the simulation, however this is dependent on the correct choice of normalisation, and by this stage the maximum has moved upstream of the viewing region. Indeed, the DMS profiles shown in figure 12(*f*), which do resolve the maximum, indicate that the experimental Fulcher emission is located ∼0.1–0.2 m poloidally upstream of the simulated emission at high density.

4.6.4. Fulcher front movement. Owing to the imprecise definition of detachment itself, as well as the fact that power, momentum and particle flux dissipation can occur at different locations along the leg, there are multiple possible definitions of the detachment 'front' [9]. A useful and experimentally measurable definition is the position where the Fulcher band emission drops to some fraction of its peak value on the target side. As shown previously [48], these 'Fulcher front' positions correlate with the positions of specific low temperatures in SOLPS-ITER simulations[28]. Indeed, in figures 12(*a*)–(*c*) (second row), there is a good correlation between the simulated 4 eV isotherm and the simulated 20% Fulcher front (black crosses), and between the 6 eV isotherm and the 50% Fulcher front (black filled circles), at least in the initial phase as the Fulcher fronts detach from the target[29]. It is therefore of interest to compare the movement of these Fulcher fronts in experiment and simulation, in response to changes in $n_{e,\mathrm{sep,OMP}}$.

Before presenting this analysis, an important caveat is that in the MWI reconstructions, the maximum Fulcher emission can move beyond the viewing region, pushing the calculated Fulcher front closer to the target than if the maximum were properly resolved. In an attempt to alleviate this effect, when the maximum was lost from the viewing region, we normalised the reconstructions to the maximum value from the previous density bin in which the maximum was successfully resolved (the assumption being that the actual maximum does not increase further once it has left the viewing region). There is considerable uncertainty in this assumption, and so the data points where it was applied are highlighted with red open circles in figures 13(*a*) and (*b*). Losing the maximum from the region of interest was less of an issue for the line of sight integrated DMS profiles, shown as black markers in figures 13(*c*)

---

[28] As discussed in [48], the peak Dα emission is a poor marker of the detachment front in strongly detached plasmas since, as seen in figure 10(*c*), the emission at low T_e can be dominated by molecule-plasma interactions.

[29] These Fulcher front positions were calculated by considering only the near-separatrix region bounded by the red flux surfaces in figures 12(*a*)–(*c*). A contour was then drawn at 20% and 50% of the maximum emission inside that region, and the front position was defined as the location on that contour where the poloidal distance to the target is minimum. The minimum distance was chosen to allow a fairer comparison between simulation and experiment, where variations in the equilibrium would make a comparison on a given flux ring less trustworthy. In reality, the Fulcher front defined in this way was found to align closely with the simulation separatrix, plotted as a black line in figures 12(*a*)–(*c*).

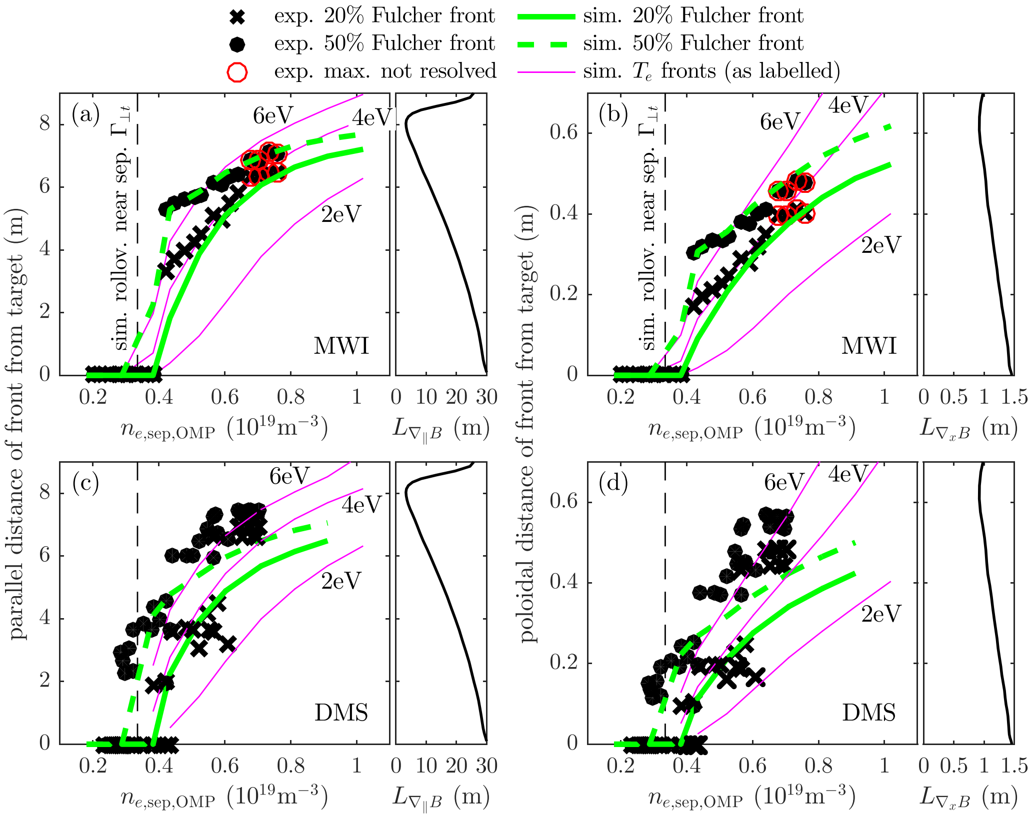

Figure 13. The evolution of the detachment front position with increasing $n_{e,\mathrm{sep,OMP}}$ in the SXD configuration, as measured by the trailing edge of the Fulcher emission, in experiment and simulation. (*a*), (*b*) Parallel (*a*) and poloidal (*b*) distance of the 20% (black crosses) and 50% (black filled circles) Fulcher fronts from the target, calculated from 2D MWI reconstructions, as a function of $n_{e,\mathrm{sep,OMP}}$. Markers surrounded by a red circle represent reconstructions for which the maximum moved beyond the viewing region (see text for details). Simulated fronts are shown in green, as labelled. (*c*), (*d*) Parallel (*c*) and poloidal (*d*) distance of the Fulcher fronts from the target, calculated from the DMS line of sight profiles. Green lines show the equivalently calculated fronts in the simulations. In all plots, the movement of the simulated electron temperature fronts (as labelled) are shown in magenta. Also shown (as a vertical black dashed line) is the $n_{e,\mathrm{sep,OMP}}$ at which the near separatrix $\Gamma_{\perp t}$ rolls over, as shown in figure 8(*a*). Additionally, next to the parallel front sensitivity plots in (*a*), (*c*), we show the local parallel gradient length scale of the magnetic field strength along the separatrix.

and (*d*), for which the maxima were always within the viewing region[30].

Figure 13 shows the movements of the 20% and 50% Fulcher fronts as a function of $n_{e,\mathrm{sep,OMP}}$, in experiment and simulation, for ((*a*) and (*b*)) the MWI reconstructions and ((*c*) and (*d*)) the DMS line of sight profiles, for ((*a*) and (*c*)) the movement in parallel space and ((*b*) and (*d*)) the movement in poloidal space. Beside each of these front sensitivity plots, we also show the local parallel or poloidal gradient length scale of the magnetic field strength along the separatrix, $L_{\nabla_\parallel B} \equiv B/(\partial B/\partial s_\parallel)$ or $L_{\nabla_x B} \equiv B/(\partial B/\partial s_x)$. The following observations can be drawn from figure 13:

- The MWI-, DMS- and simulation-derived Fulcher fronts all leave the target at similar values of $n_{e,\mathrm{sep,OMP}}$, corresponding approximately to the simulated rollover in the near separatrix $\Gamma_{\perp t}$ shown in figure 8(*a*) and marked with vertical dashed lines in figure 13.
- The sensitivity of the Fulcher front positions as they leave the target is similar in experiment and simulation and (within the experimental scatter) is consistent between MWI and DMS diagnostics.
- In parallel space, after a relatively rapid initial movement off the target, all fronts (DMS-, MWI-, and simulation-derived Fulcher fronts, as well as simulated T_e fronts) exhibit a reduced sensitivity (i.e. an increased stability) to increasing $n_{e,\mathrm{sep,OMP}}$ as they move up the leg. As recently predicted in [51], we observe a correlation between the region of reduced parallel front sensitivity and an increase in the gradient in the magnetic field strength (i.e. a reduction in $L_{\nabla_\parallel B}$). Such a 'slowing down' of the front in parallel space is also predicted by simple models [8, 9]. Physically, these models predict that it should be more 'difficult' (i.e. require a larger increase in $n_{e,\mathrm{sep,OMP}}$) to push the front up a flux tube in regions where that flux tube is narrowing rapidly and the resulting gradients in the parallel energy flux density are increased. The results presented here are the first to suggest a qualitatively similar

---

[30] The DMS viewing region extends further up the leg than the MWI viewing region, figure 10(*a*). At highest density, however, the penultimate chord from the target has the maximum line integrated emission (coloured dots in figure 13(*f*), making the accuracy of this statement dependent on the reliability of that single chord.

behaviour in experiment. However, we cannot yet rule out the possibility that the slowing may also be linked to the presence of the baffle, which is located just upstream of the region of reduced sensitivity.

- In poloidal space, the change in stability of the front as it moves up the leg is less pronounced. This is consistent with the reduced variation in $L_{\nabla_x B}$ compared to the strong variation in $L_{\nabla_\parallel B}$; variation in the latter is driven primarily by the field line becoming more aligned with the major radial direction (in which B changes maximally) as the baffle region is approached (recall figure 2).
- The simulations suggest that the 20% and 50% Fulcher fronts track the 4 eV and 6 eV T_e fronts well until they reach a parallel (poloidal) distance of ~5 m (0.4 m) from the target. Beyond this distance, the simulated Fulcher fronts start to correspond to slightly lower values of T_e, as shown. As a result, the reduced sensitivity further up the leg, detailed in the previous two bullets, is less apparent (though still present) for the T_e fronts compared to the Fulcher fronts. Due to the changing magnetic pitch along the leg, this is particularly true in poloidal space.

It is important to note that the experimental front positions presented here can be affected by the same strike point splitting that affected our analysis of the target quantities in sections 4.4 and 4.5. The splitting is less obvious in the averaged reconstructions shown in figures 12(*a*)–(*c*), but one can question the degree to which the averaging of split reconstructions brings us closer to the result if there were no splitting. For now, this question remains an open one, although the reasonable level of agreement with simulations at low and mid densities seen in this section demonstrates that the strike point splitting in experiment does not shift us completely away from the toroidally symmetric physics assumed by the code.

5. Discussion

5.1. Analysis of the upstream separatrix temperature

In section 4.1, it was shown that the simulated $T_{e,\mathrm{sep,OMP}}$ drops considerably as a function of $n_{e,\mathrm{sep,OMP}}$, and that this was in line with the experimental trend (based on the Thomson data and with a constant 0.5 cm inward shift of the EFIT-derived separatrix position). The simulated $T_{e,\mathrm{sep,OMP}}$ vs. $n_{e,\mathrm{sep,OMP}}$, for CD and SXD simulations, is plotted again in figure 14(*a*) (solid lines), now including simulations with drift terms deactivated, as well as the corresponding (lower outer) target separatrix electron temperature, $T_{e,\mathrm{sep},t}$ (dashed lines). The observed reduction in $T_{e,\mathrm{sep,OMP}}$ requires explanation, since no density dependence is expected if the separatrix parallel plasma energy flux density, $Q_{\parallel,\mathrm{sep,plasma}}$, is density-independent and dominated by electron conduction, and if $T_{e,\mathrm{sep},t}$ is negligible.

To understand the simulated reduction in $T_{e,\mathrm{sep,OMP}}$, figure 14(*b*) shows a more detailed analysis for the CD fuelling scan with drifts turned off (since drifts have little impact on the $T_{e,\mathrm{sep,OMP}}$ vs. $n_{e,\mathrm{sep,OMP}}$ plots shown in figure 14(*a*), we focus our analysis in figures 14(*b*)–(*d*) on the simpler case without drifts). Each coloured line shows a post-calculated two-point model [36] calculation for $T_{e,\mathrm{sep,OMP}}$, starting from an equation that agrees well with the simulations and progressively including approximations that are often made when approximating $T_{e,\mathrm{sep,OMP}}$. Table 1 lists the formulae used for each line.

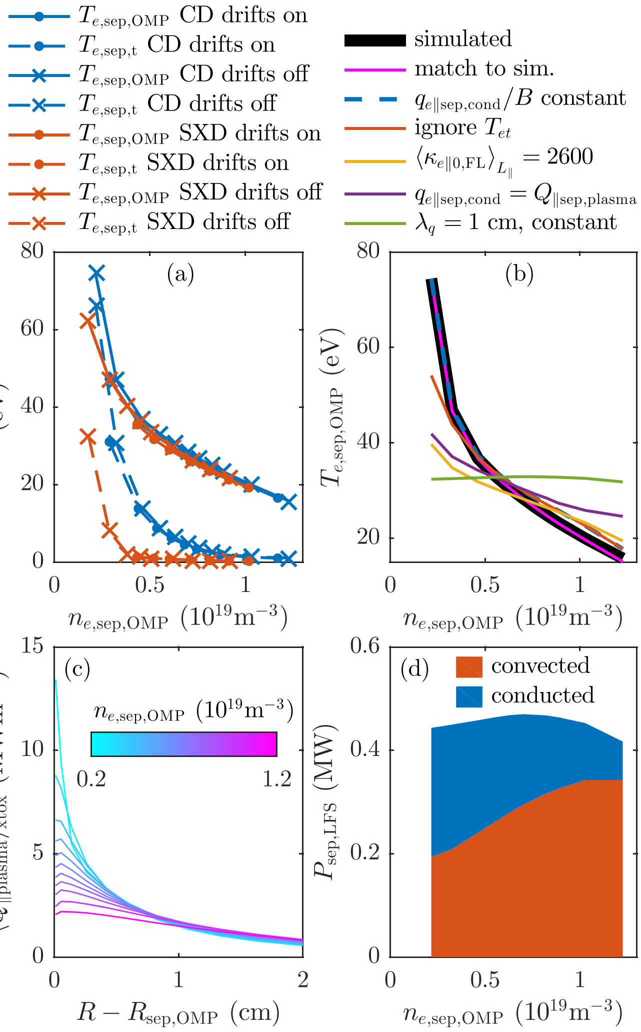

Figure 14. Understanding the simulated reduction in $T_{e,\mathrm{sep,OMP}}$ with increasing $n_{e,\mathrm{sep,OMP}}$. (*a*) The simulated target and OMP T_e values, in CD and SXD, with drift terms on and off, as labelled. (*b*) Analysis of the CD no drift scan, with increasingly realistic two-point model post calculations of $T_{e,\mathrm{sep,OMP}}$ (see text and table 1 for details). (*c*) Simulated parallel-averaged (between the two X-points) parallel plasma energy flux density for CD no drift scan, showing significant reduction in the near SOL values with increasing $n_{e,\mathrm{sep,OMP}}$. (*d*) Convected vs. conducted radial power crossing the LFS separatrix for CD no drift scan. The flux becomes increasingly dominated by convection with increasing $n_{e,\mathrm{sep,OMP}}$.

For the magenta solid line (‘Match to sim.’ in table 1), the formula is essentially a rearrangement of the definition of the electron conducted parallel energy flux density in the simulation. It therefore matches well to the simulated $T_{e,\mathrm{sep,OMP}}$. Here,

Table 1. Detailed list of formulae used for the lines plotted in figure 14(*b*).

Legend entry	Formula	Notes
Match to sim.	$\left(\frac{7}{2}\frac{\langle q_{e\parallel\text{sep,cond}}\rangle_{L_\parallel}L_\parallel}{\langle\kappa_{e\parallel 0,\text{FL}}\rangle_{L_\parallel}}+T_{e,\text{sep},t}^{7/2}\right)^{2/7}$	Essentially a rearrangement of the definition of $q_{e\parallel\text{sep,cond}}$ in the simulation → good agreement between formula and simulation.
$q_{e\parallel\text{sep,cond}}/B$ constant	$\left(\frac{7}{2}\frac{\langle q_{e\parallel\text{sep,cond}}\rangle_{L_{\parallel\text{x}}}C_BL_\parallel}{\langle\kappa_{e\parallel 0,\text{FL}}\rangle_{L_\parallel}}+T_{e,\text{sep},t}^{7/2}\right)^{2/7}$	Includes the impact of assuming no power losses along the leg to reduce $q_{e\parallel\text{sep,cond}}$.
Ignore T_{et}	$\left(\frac{7}{2}\frac{\langle q_{e\parallel\text{sep,cond}}\rangle_{L_{\parallel\text{x}}}C_BL_\parallel}{\langle\kappa_{e\parallel 0,\text{FL}}\rangle_{L_\parallel}}\right)^{2/7}$	Includes the impact of assuming negligible target temperature.
$\langle\kappa_{e\parallel 0,\text{FL}}\rangle_{L_\parallel}=2600$	$\left(\frac{7}{2}\frac{\langle q_{e\parallel\text{sep,cond}}\rangle_{L_{\parallel\text{x}}}C_BL_\parallel}{2600}\right)^{2/7}$	Includes the impact of assuming constant $\kappa_{e\parallel 0}$.
$q_{e\parallel\text{sep,cond}}=Q_{\parallel\text{sep,plasma}}$	$\left(\frac{7}{2}\frac{\langle Q_{\parallel\text{sep,plasma}}\rangle_{L_{\parallel\text{x}}}C_BL_\parallel}{2600}\right)^{2/7}$	Includes the impact of assuming that all of the parallel energy flux density is conducted by electrons.
$\lambda_q=1$ cm, constant	$\left(\frac{7}{2}\frac{\left(P_{\text{sep,LFS}}/2/\langle A_\parallel\rangle\right)C_BL_\parallel}{2600}\right)^{2/7}$	Uses a fixed λ_q to calculate $Q_{\parallel\text{sep,plasma}}$; $T_{e,\text{sep,OMP}}$ varies only because of changes in $P_{\text{sep,LFS}}$.

$$\langle q_{e\parallel\text{sep,cond}}\rangle_{L_\parallel}\equiv\frac{1}{L_\parallel}\int_{\text{OMP}}^{\text{LOT}}q_{e\parallel\text{sep,cond}}\text{d}s_\parallel \tag{5}$$

is the parallel average of the parallel electron conducted energy flux density along the first SOL ring of the simulation, $q_{e\parallel\text{sep,cond}}$ (LOT stands for 'lower outer target'). For the flux-limited $\kappa_{e\parallel 0}$, we take an average weighted by $q_{e\parallel\text{sep,cond}}$:

$$\langle\kappa_{e\parallel 0,\text{FL}}\rangle_{L_\parallel}\equiv\frac{\int_{\text{OMP}}^{\text{LOT}}\kappa_{e\parallel 0,\text{FL}}q_{e\parallel\text{sep,cond}}\text{d}s_\parallel}{\int_{\text{OMP}}^{\text{LOT}}q_{e\parallel\text{sep,cond}}\text{d}s_\parallel}. \tag{6}$$

Here, $\kappa_{e\parallel 0,\text{FL}}$ is the parallel electron heat conductivity divided by $T_e^{5/2}$ after the flux limiting procedure has been applied.

For the blue dashed line, we make an assumption that there are no losses between the X-point and the target; $q_{e\parallel\text{sep,cond}}$ drops only because of the decreasing magnetic field strength, i.e.

$$\langle q_{e\parallel\text{sep,cond}}\rangle_{L_\parallel}\approx\langle q_{e\parallel\text{sep,cond}}\rangle_{L_{\parallel\text{x}}}C_B, \tag{7}$$

where

$$\langle q_{e\parallel\text{sep,cond}}\rangle_{L_{\parallel\text{x}}}\equiv\frac{1}{L_{\parallel\text{x}}}\int_{\text{OMP}}^{\text{LX}}q_{e\parallel\text{sep,cond}}\text{d}s_\parallel \tag{8}$$

and

$$C_B\equiv\frac{\int_{\text{OMP}}^{\text{OT}}B\text{d}s}{\int_{\text{OMP}}^{\text{LX}}B\text{d}s}. \tag{9}$$

Comparing this blue dashed line to the magenta solid line, we see that this assumption results in a slight overestimate of $T_{e,\text{sep,OMP}}$ at high $n_{e,\text{sep,OMP}}$, as losses in the divertor increase. The effect is small, however, since these losses occur sufficiently close to the target[31].

For the red solid line, we make a further assumption that $T_{e,\text{sep},t}$ can be ignored in the calculation. This is valid when $T_{e,\text{sep},t}^{2/7}\ll T_{e,\text{sep,OMP}}^{2/7}$, which is not the case at low density (recall the dashed lines in figure 14(*a*). As a result, applying this assumption acts to significantly reduce the $T_{e,\text{sep,OMP}}$ as the SOL becomes sheath limited at low collisionality (compare red solid and blue dashed lines).

For the yellow solid line, we further assume that the effect of flux limiting on the electron parallel conductivity can be ignored, so that $\langle\kappa_{e\parallel 0,\text{FL}}\rangle_{L_\parallel}\approx 2600\ \text{Wm}^{-1}\text{eV}^{-7/2}$. In reality, as collisionality reduces, the heat flux upstream self limits at some fraction of the free streaming heat flux [32, 36], reducing the effective $\kappa_{e\parallel 0}$ (a reality that is modelled in our fluid simulations via parallel heat flux limiters). The assumption that this can be ignored results in a decrease in the calculated $T_{e,\text{sep,OMP}}$ at low $n_{e,\text{sep,OMP}}$ and a reduction in the overall drop in $T_{e,\text{sep,OMP}}$ across the scan (compare yellow solid to red solid lines).

For the purple solid line, we further assume that all of the parallel plasma energy flux is electron conducted, i.e. that $q_{e\parallel\text{sep,cond}}=Q_{\parallel\text{sep,plasma}}$. Comparing this to the previous yellow solid line, we see that this assumption acts to increase the calculated $T_{e,\text{sep,OMP}}$, particularly at high $n_{e,\text{sep,OMP}}$ where the parallel convection energy channel becomes of similar order to the electron conduction channel.

Finally, for the green solid line, we further assume that there is no change in radial transport through the scan; the plasma energy flux width remains fixed at $\lambda_q=1$ cm. The resulting upstream energy flux, $\left(P_{\text{sep,LFS}}/2/\langle A_\parallel\rangle\right)$, changes only due to changes in $P_{\text{sep,LFS}}$ which, as seen in figure 14(*d*), are small (here, $A_\parallel=2\pi R_{\text{sep,OMP}}\lambda_q\left(B_{\text{sep,OMP}}/B_{x\text{sep,OMP}}\right)$, where

---

[31] Movement of the detachment front away from the target has only a weak effect on $T_{e,\text{sep,OMP}}$ since it acts to reduce the effective $L_\parallel$, and $T_{e,\text{sep,OMP}}\sim L_\parallel^{2/7}$.

B_x is the poloidal field strength). As a result of this final assumption, the calculated $T_{e,\mathrm{sep,OMP}}$ exhibits practically no variation through the density scan, indicating that increasing radial energy transport through the scan acts to significantly reduce $T_{e,\mathrm{sep,OMP}}$ (compare purple to green solid lines)[32].

Why does the simulated radial transport increase so strongly? The effect must be strong in order to affect the $T_{e,\mathrm{sep,OMP}}$ calculation, since $T_{e,\mathrm{sep,OMP}} \propto Q_{\parallel\mathrm{sep,plasma}}^{2/7}$. Figure 14(*c*) shows that, indeed, there is a large drop in $Q_{\parallel\mathrm{sep,plasma}}$ due to increased transport as $n_{e,\mathrm{sep,OMP}}$ increases. To understand this, consider that, in a SOL whose radial and parallel energy transport is dominated by conduction, the SOL width can be approximated from power balance as (equation (5.72) in [36]):

$$\lambda_{q\parallel} \approx \left(\frac{e n_{e,\mathrm{sep,OMP}} \chi_\perp}{\kappa_{e\parallel 0} T_{e,\mathrm{sep,OMP}}^{5/2}}\right)^{1/2} L_\parallel, \tag{10}$$

where $\chi_\perp$ is the anomalous perpendicular conduction coefficient ($= 4\ \mathrm{m^2\,s^{-1}}$ in these simulations). For the lowest density CD simulation (without drifts), (10) gives $\lambda_{q\parallel} \approx 2.6$ mm, similar to the near SOL fall off length shown in figure 14(*c*) at lowest density. As the fuelling increases, however, the power crossing the LFS separatrix becomes increasingly dominated by convection (figure 14(*d*)). In this regime, we expect $\lambda_{q\parallel}$ to tend towards λ_n, given by particle balance as[33]:

$$\lambda_n \approx \frac{n_{e,\mathrm{sep,OMP}} D_\perp A_{\mathrm{sep,LFS}}}{\Gamma_{\mathrm{IZ,core}}}, \tag{11}$$

where $D_\perp$ is the anomalous perpendicular diffusion coefficient ($= 4\ \mathrm{m^2\,s^{-1}}$ in these simulations), $A_{\mathrm{sep,LFS}}$ is the area of the LFS separatrix (from X-point to X-point; $= 20.6\ \mathrm{m^2}$ here), and $\Gamma_{\mathrm{IZ,core}}$ is the volume integrated ionisation source on closed field lines. For the highest density CD simulation (without drifts; $\Gamma_{\mathrm{IZ,core}} = 2.9 \times 10^{22}\ \mathrm{s^{-1}}$), (11) gives $\lambda_n \approx 35$ mm, similar to the fall off length at high density in figure 14(*c*). Thus, the increased transport that acts to reduce $T_{e,\mathrm{sep,OMP}}$ is a consequence of moving from a conduction-dominated to a convection-dominated regime. Interestingly, the wide range of $\lambda_{q\parallel}$ on display in figure 14(*c*) is in line with experimental analysis from MAST [52], which reported $\lambda_{q\parallel}$ values between ~4 mm and ~30 mm, with a strong scaling with line averaged density (to the power 1.52 ± 0.16). Our results suggest that this strong scaling might be explained by fixed anomalous transport coefficients, combined with a transition to a convection dominated regime.

We deduce from the above that increased radial convection, in addition to the increased parallel convection mentioned above, acts to further reduce the calculated $T_{e,\mathrm{sep,OMP}}$, particularly at high $n_{e,\mathrm{sep,OMP}}$. In the case where radial convection dominates the power through the separatrix, both of these processes must act to satisfy

$$\begin{aligned} P_{\mathrm{sep,LFS}} &\approx P_{\mathrm{sep,LFS,conv}} \\ &\approx \frac{5}{2}\Gamma_{\mathrm{IZ,core}} T_{e,\mathrm{sep,OMP}} \left(1 + \frac{T_{i,\mathrm{sep,OMP}}}{T_{e,\mathrm{sep,OMP}}}\right), \end{aligned} \tag{12}$$

i.e. (for fixed $T_{i,\mathrm{sep,OMP}}/T_{e,\mathrm{sep,OMP}}$ and $P_{\mathrm{sep,LFS}}$) $T_{e,\mathrm{sep,OMP}}$ is inversely proportional to the total ionisation source on closed field lines, which itself is approximately proportional to the puff rate and to $n_{e,\mathrm{sep,OMP}}$. This is also in line with experimental data on TCV, in which a strong reduction in $T_{e,\mathrm{sep,OMP}}$ was reported with increasing density [53][34].

Finally, consider the (lack of) difference in $T_{e,\mathrm{sep,OMP}}(n_{e,\mathrm{sep,OMP}})$ between CD and SXD. This is consistent with the factor 1.3 increase in $L_\parallel$ in SXD, implying only a factor $1.3^{2/7} = 1.08$ increase in $T_{e,\mathrm{sep,OMP}}$. The main difference between the two configurations occurs at low density, where the CD has a higher $T_{e,\mathrm{sep,OMP}}$ because it enters into sheath-limited regime at higher $n_{e,\mathrm{sep,OMP}}$ (see also [13]). We note, however, that the experimental evidence does not appear to suggest a higher $T_{e,\mathrm{sep,OMP}}$ in CD at low density (figure 4(*b*)).

5.2. Reduction of the peak target heat load in the Super-X configuration

It was shown in figure 9(*b*) that the peak heat load to the lower outer target in the SXD is a factor 26.8 lower than in the CD, at comparable $n_{e,\mathrm{sep,OMP}}$. Factors of 4.9, 1.9 and 2.9 reduction were due to the SXD having increased poloidal flux expansion, toroidal flux expansion and volumetric dissipation, respectively. Given that poloidal flux expansion is relatively easy to increase compared to the target major radius, the additional factor 2.9 reduction due to increased dissipation in the SXD is an important added benefit which we now analyse further.

Figure 15(*a*) (left axis) shows the cumulative power dissipation fractions in the lower outer divertor, as a function of the parallel distance from the X-point[35], for the (second) SOL flux ring at which the heat load is peaked, in the CD-MD (solid black line) and SXD-HD (dashed black line) simulations. The T_e profiles for the same two simulations are also

---

[32] The effect of upstream neutral energy losses on $T_{e,\mathrm{sep,OMP}}$ was also calculated, but was found to be negligible, at least for the converged simulations shown here. When the simulations were pushed to even higher density, neutral losses from the core drove a collapse in the upstream plasma pressure, and a steady state solution could not be found (see section 5.4).

[33] Assuming the majority of ions leaving closed field lines cross the LFS separatrix.

[34] It is important to recognise that equation (12), and the strong reduction in $T_{e,\mathrm{sep,OMP}}$ that it implies, is only relevant for relatively low powered, neutrally transparent discharges (for which a large fraction of the puffed and recycled neutrals are ionised on closed field lines). On ITER, by contrast, the pellet fuelling is expected to provide an ion source of $\sim 10^{22}\ \mathrm{s^{-1}}$, with very little ionisation on closed field lines besides [12]. For typical values of $T_{e,\mathrm{sep,OMP}} = 150$ eV and $T_{i,\mathrm{sep,OMP}}/T_{e,\mathrm{sep,OMP}} = 2$, this gives $P_{\mathrm{sep,LFS,conv}} = 1.8$ MW, which is negligible compared to the expected power through the separatrix of 100 MW.

[35] Note that the target distances on this plot are shorter than the $L_\parallel$ values plotted in figure 2(*e*) because $L_\parallel$ is measured from the OMP.

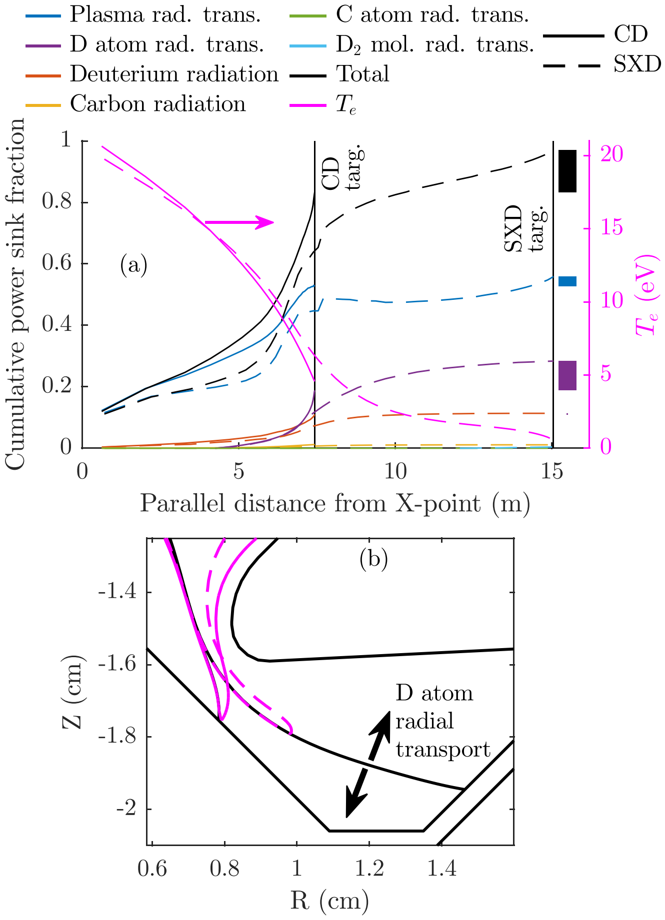

Figure 15. (a) Power dissipation mechanisms along the (second SOL) lower outer divertor flux tube at which the target heat load is maximum, in CD (CD-MD) and SXD (SXD-HD) simulations, which have comparable upstream conditions. Also shown on the right axes are the electron temperature profiles along the same flux tube. The target locations in the two configurations are given by the appropriately labelled vertical lines. For each mechanism, the difference in the cumulated power sink fractions between the two simulations are given by the heights of coloured vertical lines to the right of the SXD target location (these are drawn from the respective solid line's y-value at the CD target to the dashed line's y-value at the SXD target). (b) The $T_e = 5$ eV contours in the two simulations (solid: CD, dashed: SXD), indicating the importance of net D atom radial transport out of the critical flux tube, for which there is room in the SXD.

shown (right axis). These are the same simulations shown previously in figure 9 and have comparable upstream profiles, including similar $n_{e,\mathrm{sep,OMP}}$ and $T_{e,\mathrm{sep,OMP}}$, as well as comparable $Q_{\|\mathrm{plasma}}$ at the divertor entrance. We define this cumulative power dissipation fraction as the cumulative power loss along the flux ring (zero at the divertor entrance), divided by the poloidal energy flux entering the flux ring at the divertor entrance. Note that we are discussing here the dissipation of the *total* poloidal energy flux from this critical flux ring (including plasma kinetic and neutral kinetic contributions, as well as the potential energy of ions to combine with electrons to form atoms and the potential energy of D atoms to combine with each other to form D$_2$ molecules). The components of this dissipation are provided in figure 15(a), as labelled[36]. For both simulations, these components sum to the black lines.

The upstream density chosen for the comparison in figure 15(a) is particularly interesting. The CD simulation is on the verge of detaching ($T_e = 4.5$ eV at the target, near separatrix $\Gamma_{\perp t}$ just rolling over), while the SXD simulation is deeply detached with its 5 eV front near the location of the CD target, but reaching a much lower temperature of $T_{et} = 0.5$ eV at the target. We see that the T_e and loss profiles in both simulations are similar up to the location of the CD target, suggesting that, for a given $n_{e,\mathrm{sep,OMP}}$ and $Q_{\|\mathrm{plasma}}$ at the divertor entrance, the plasma profiles upstream of $T_e \approx 5$ eV are governed primarily by the geometry upstream of $T_e \approx 5$ eV, which are similar in CD and SXD (recall figure 2)[37].

In both configurations, the dominant loss mechanism from this critical flux ring (responsible for ~50% of the reduction in energy flux from divertor entrance to target) is net plasma radial transport (blue lines labelled 'plasma rad. trans.' in the legend). Deuterium radiation (red) and net radial deuterium atom transport (purple) are also significant, while carbon radiation (yellow) is a negligible power loss mechanism for these plasmas[38]. Dissipation through net radial carbon atom (green) and D$_2$ molecule transport (light blue) is also negligible in these simulations.

Importantly, in both configurations, the losses due to plasma radial transport and deuterium radiation occur primarily *upstream* of the CD target location, where the plasma profiles are similar. As a result, the total loss fraction incurred via these processes is also similar in the two configurations; on the target side of the $T_e \approx 5$ eV front, radial plasma gradients are too small and electron temperatures are too low for these mechanisms to reduce the total poloidal energy flux any further.

Where the SXD has an advantage over the CD, however, is in the additional dissipation by net radial transport of energy carried by atoms (purple) out of the critical flux tube, in the additional space that it provides downstream of the CD target location. In figure 15(a), the increased loss from the entire SXD critical flux tube (compared to the CD), due to the different mechanisms, is given by the height of the respective coloured bars just to the right of the SXD target location; the height of the blue and red bars is small compared to the

---

[36] The total poloidal energy flux can only be reduced via the net radial transport of energy out of the flux ring, either of photons ('deuterium radiation' or 'carbon radiation' in figure 15(a), of the kinetic and potential energy of the plasma ('plasma rad. trans.'), or of the kinetic and potential energy of the neutrals ('D atom rad. trans.', 'C atom rad. trans.' and 'D$_2$ mol. rad. trans.'). The accumulation of these losses is what is plotted.

[37] Recent experimental results from MAST-U suggest that, once off the target, the $T_e \approx 5$ eV front is indeed independent of the magnetic geometry downstream of it [54].

[38] Given the acceptable level of absolute agreement between simulated and measured CIII (465 nm) emissivity (see appendix C), we infer that carbon radiation is also negligible in experiment, at least in the lower outer divertor. This has been further confirmed in recent SXD experiments by comparing the bolometry-inferred total radiation in the lower outer divertor to the spectroscopy-inferred deuterium radiation [55].

purple. Thus, net radial atom transport is the one loss mechanism that does increase downstream of the CD target location, and is responsible for the additional dissipation in the SXD. This increases significantly, from 0.11 of the incoming power at the location of the CD target to 0.28 of the incoming power at the location of the SXD target. Although this may not seem that significant compared to the dominant losses that occur upstream of the CD target location, when extrapolated to a reactor, this difference between dissipating 83% of power from the critical flux tube in the CD, vs. near total dissipation in the SXD could be the difference between melting the target or not. On MAST-U, it is the reason for the additional 2.9 times reduction in the peak heat load in SXD for these simulations.

An important proviso should be made on the above analysis, that recent work [42] suggests the creation of D_2^+ ions via molecular charge exchange may be underestimated in the default SOLPS-ITER neutral model used in these simulations. This in turn may result in an underestimate in the atomic deuterium radiation in regions where $T_e \lesssim 5$ eV, potentially adding an important power loss mechanism not captured here. This will be investigated further in future work.

5.3. *Divertor ion particle balance*

One of the starkest differences between the SXD and CD simulations, observed in figure 8(*b*), is that the total ion fluxes to the outer targets saturate and roll over earlier in the SXD. In fact, in the CD simulations, the total target ion flux does not reduce at all (at least not stably; see section 5.4). To understand this, in figure 16 we plot the ion balance, integrated over the upper and lower outer divertors, in CD (*a*) and SXD (*b*) simulations.

Consider first the sources of ions in the outer divertors due to neutral-plasma interactions. These occur due to electron impact ionisation of atoms (purple lines in figures 16(*a*) and (*b*)), as well as molecular-assisted processes (green lines). The latter include both molecular-assisted ionisation (MAI), i.e. ion conversion followed by dissociative ionisation (an ion source), as well as molecular-assisted recombination (MAR), i.e. ion conversion followed by dissociative recombination (an ion sink). In the CD simulations, we observe that the neutral sources of deuterium ions in the outer divertors do roll over with increasing $n_{e,\mathrm{sep,OMP}}$. However, this does not result in a rollover of the flux to the targets, due to significant particle fluxes crossing into the divertors from upstream (darker blue lines). These fluxes result from ionisation upstream of the outer divertors, in the core and outer main SOL (OMS; between the two outer divertor entrances).

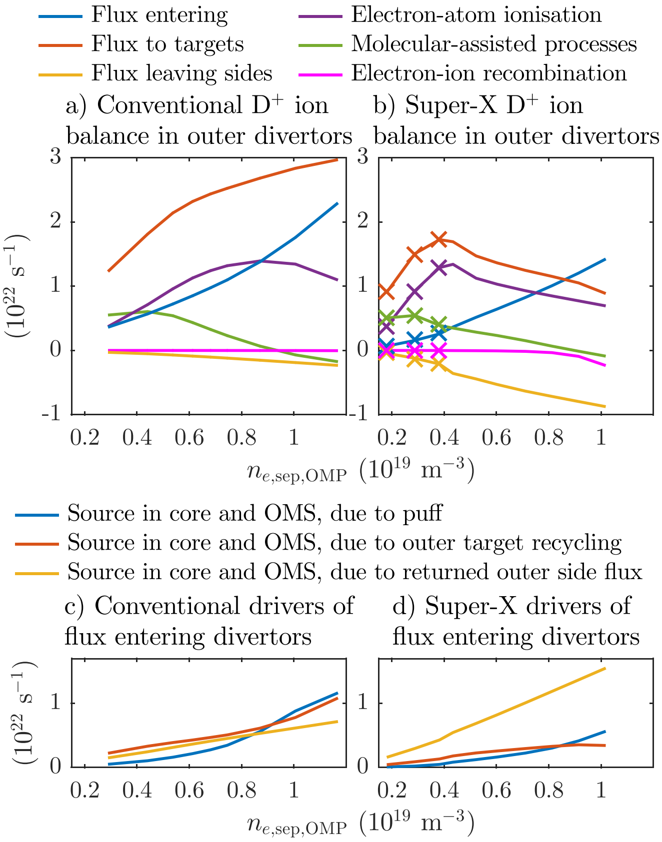

Figure 16. Total deuterium ion particle balance in combined upper and lower outer divertors, in CD (*a*) and SXD (*b*) simulations. Crosses represent simulations without drifts. The contributors to the fluxes entering the outer divertors, i.e. ionisation upstream of the divertors in the core and outer main SOL (OMS), are shown in figures (*c*) and (*d*). These are decomposed according to the starting location of the neutrals.

Figure 16(*c*) shows the components of this upstream ionisation in the CD configuration, decomposed according to the starting location of the neutrals, as labelled. We see that the flux entering the divertor is driven by a combination of the following: neutrals puffed into the chamber which cross over the separatrix (blue), neutrals recycled from the outer targets which escape the outer divertors (red), and neutrals returned from the outboard radial side of the numerical grid (yellow)[39]. Note that, if the puff were not such a significant fraction of the target flux, then the simulated flux to the targets would saturate around $n_{e,\mathrm{sep,OMP}} \approx 0.8 \times 10^{19}\ \mathrm{m}^{-3}$ (all else being equal). Importantly, though, the target flux would not roll over; the total neutral source, excluding puffing (i.e. the sum of the purple and green lines in figure 16(*a*) and the red and yellow lines in figure 16(*c*) saturates due to power starvation, but does not roll over without recombination (either molecular-activated or electron-ion). Neither of these are significant in the CD simulations (for the default set of neutral rates and input power used).

By contrast, in the SXD simulations (figure 16(*b*)), the neutral sources in the outer divertors saturate around $n_{e,\mathrm{sep,OMP}} \approx 0.4 \times 10^{19}\ \mathrm{m}^{-3}$, at which point the fluxes entering the divertor (in particular due to the lower puff rate) are insufficient to stop

---

[39] We used the default SOLPS-ITER setting here, whereby the ion fluxes leaving the radial sides of the grid are returned as atoms with the local ion temperature.

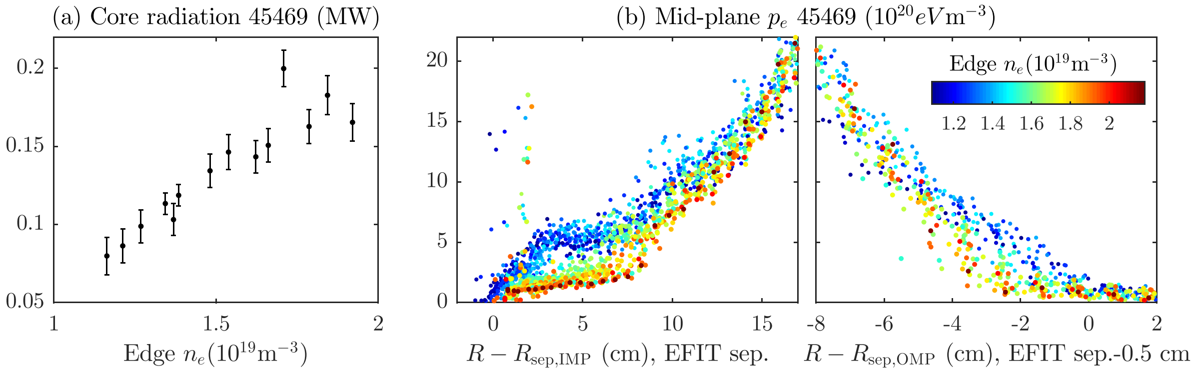

Figure 17. Evidence of mid-plane separatrix electron pressure reduction with increasing edge density and core radiation in the CD configuration at highest density (shot 45469). (*a*) IRVB-derived radiation inside the separatrix with increasing edge n_e. (*b*) Thomson scattering profiles of the electron pressure at the inboard (left) and outboard (right) mid-plane, as a function of the major radial distance past the EFIT-derived separatrix (shifted inwards by 0.5 cm for the outboard side, as justified in section 4.1).

the target flux from saturating as well. The subsequent reduction in total ion flux appears to be mostly driven by a significant radial ion flux from the radial sides of the numerical grid; the recombination sink, plotted in magenta in figure 16(*b*), is small even for the highest density simulations. Recall from the discussion of figure 2(*b*) that the SXD grid was limited by an additional null point on the underside of the baffle. This limited the radial width of the SOL to 2.5 cm at the OMP (compared to 4.6 cm for the CD grid). Given that the fluxes leaving the sides are dependent on our choice of boundary condition and radial transport coefficients, for which there is considerable uncertainty, it is difficult to know whether the experimental reduction in the SXD total outer target flux (recall figure 8(*b*)) is due to radial ion transport away from the target areas covered by Langmuir probes, or whether in fact the reduction observed in experiment is driven by additional volumetric recombination processes that are not present in the current simulations. Future work should focus on simulating equilibria for which the SXD grid is limited by the baffle. Simulations with grids extended to the walls of the SXD chamber would also be of interest. It is important to note, however, that we do not expect the results relating to near separatrix quanties in the SXD simulations, discussed in this paper, to be significantly changed by improvements to the far SOL model.

As mentioned previously, it is possible that the simulations presented here undervalue the creation of D_2^+ molecules in the divertors, and thus also the reduction target fluxes due to MAR [42]. This could potentially explain both the lack of target rollover in CD as well as the apparently less substantial rollover in SXD. An investigation into the sensitivity of the simulations to these rates is intended for future work. There is, however, an additional mechanism we suspect is also acting to reduce the experimentally measured target flux in the CD configuration, which will be discussed in the next section.

5.4. Radiative collapse due to neutral losses inside the separatrix in the Conventional configuration

In figure 8, only simulations that converged to a steady state were shown. As reported in section 4.3, the inner mid-plane separatrix electron temperature was just 2.6 eV for the highest density converged simulation with HFS fuelling. When the simulations were pushed to higher fuelling, they entered an unstable collapse, whereby the radiation and ionisation losses from deuterium neutrals crossing the separatrix reduced the inner separatrix temperature even further, in turn allowing more neutrals to cross. During this collapse, the power available for ionisation of ions that ultimately reach the outer targets is diminished, and the outer target fluxes collapse. Concomitant with these strong core power losses is an unstable degradation of the simulated upstream plasma pressure, not only at the inner mid-plane separatrix in the vicinity of the puff, but at the OMP separatrix as well[40].

Figure 17 provides evidence for a similar separatrix pressure degradation in experiment, for the highest density CD shot (45469). The strong reduction in total upper target particle flux observed experimentally in the CD configuration comes almost entirely from this shot (darker blue dots in figure 8(*b*). As seen in figure 17(*a*), the IRVB-derived radiation[41] from inside the (EFIT-derived) separatrix increases with increasing edge density (we use the same definition for edge density here as in section 4.1). It is highly likely that the plotted values are in fact an underestimate of the actual radiation inside the separatrix, since the trusted IRVB field of view does not cover the region near the HFS puff (where we expect the most significant radiation) and so does not include this region in the radiated power calculation. We can conclude that, at highest density, the radiation inside the separatrix approaches approximately half the ohmic heating power of ∼0.6 MW. At the same time, as seen in figure 17(*b*), there is a significant reduction in the electron pressure measured by Thomson scattering, especially on the inboard side, but also on the outboard side, as the edge density increases.

---

[40] One can also view this radiative collapse through the prism of equation (12), which states that the separatrix temperature must drop inversely with the ionisation source on closed field lines, in order for power and particle balance to be satisfied when the radial power flux is dominated by convection.

[41] The IRVB diagnostic covers only the lower half of the tokamak. In figure 17(*a*) the IRVB-derived radiation inside the separatrix has been doubled to estimate the total.

Based on the above, we postulate that the experimental rollover in the CD configuration (figure 8) may be attributed, at least in part, to an upstream pressure degradation driven by deuterium neutral losses inside the separatrix[42]. We are primarily interested, however, in the more reactor-relevant form of target flux rollover, driven by volume recombination in the divertor rather than power starvation in the core (and concomitant upstream pressure degradation). It is therefore of interest to explore in the simulations what is required to achieve this more reactor-relevant (and, in the simulations at least, stable) target flux rollover.

Figure 18 shows the effect of switching the simulated puff location from the HFS to the LFS and of increasing the input power from 0.6 MW to 2.0 MW, on (*a*) the simulated outer target flux (summed over upper and lower targets), and (*b*) the integrated electron-ion recombination (EIR) in the outer divertors. Since, for the default scan (blue lines), a considerable fraction of the power sink inside the separatrix is caused by neutrals originating from the HFS puff (∼half for the last stable CD simulation), one would expect that switching the location of the gas puff to the LFS (red lines) should impact the rollover behaviour. Indeed, the unstable collapse of the simulations occurs at a 41% higher $n_{e,\mathrm{sep,OMP}}$ for the LFS-fuelled cases. However, there is still a collapse of the simulations, driven by neutrals escaping to the core from the divertors before the divertor density is high enough for EIR to take place.

Increasing the input power acts to increase the electron density in the divertors, promoting three-body EIR in the divertor volume (a strongly increasing function of n_e for $T_e \lesssim 5$ eV) and reducing the mean free path of escaping neutrals. If the simulation is still fuelled from the HFS, however, then we still observe an unstable collapse due to puffed neutrals crossing the inboard separatrix (purple lines in figure 18). Only through a combination of LFS fuelling *and* increased input power (green line) can a stable reduction of the target flux be obtained due to divertor volume recombination. This motivates experiments with increased input power and LFS fuelling, which may only be possible in ELM-y H-mode.

5.5. Effect of drifts and currents

In general, the important trends assessed in this paper[43] are insensitive to the inclusion of drifts (although there are some effects on the detailed profiles of n_e and T_e in the divertors). At higher P_{in}, however, the impact of drifts can become more pronounced. With this in mind, we now present an initial assessment of the impact of drift and current terms on up-down power asymmetries (we focus on the up-down asymmetry here since, in connected double null geometry, the in-out asymmetry is expected to be driven primarily by the ballooned nature of turbulence, which is not simulated).

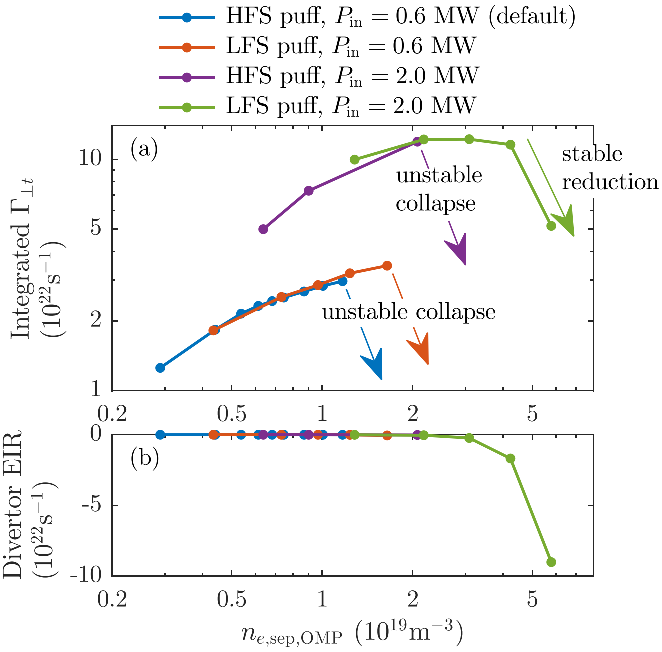

Figure 18. The simulated effect of fuelling location and increased input power on (*a*) the outer target flux and (*b*) the integrated electron-ion recombination in the outer divertors, in CD configuration, as a function of $n_{e,\mathrm{sep,OMP}}$.

Figure 19 shows the total power to the upper target divided by the total power to the lower target, for (a) the inner targets and (b) the outer targets, for the CD and SXD configurations and for the additional CD scans shown in figure 18, as labelled[44]. At $P_{\mathrm{in}} = 0.6$ (i.e. input powers relevant to the experimental data assessed in this paper), there is little up-down power asymmetry in the simulations. However, for the higher $P_{\mathrm{in}} = 2.0$ MW (predictive) simulations, there is significant inner and outer up-down asymmetry at low density, which reduces with increasing density.

To understand this behaviour, we focus on the CD (HFS puff, $P_{\mathrm{in}} = 2.0$ MW) simulation highlighted with a purple open circle in figure 19(*b*). The radially integrated poloidal plasma energy flux densities (units MW after radial integration) as a function of poloidal distance[45], are shown for the HFS SOL and for the LFS SOL in figures 20(*a*) and (*e*),

---

[42] It is worth noting that the apparently steady reduction in the integrated measured $\Gamma_{\perp t}$ shown in figure 8(*b*) might be a much sharper function of the actual experimental $n_{e,\mathrm{sep,OMP}}$. Recall from section 4.1 that the inferred $n_{e,\mathrm{sep,OMP}}$ on the x-axis of figure 8 results from a shifting of the Thomson profiles in order to match the simulated $T_{e,\mathrm{sep,OMP}}(n_{e,\mathrm{sep,OMP}})$. If, in fact, there is a faster drop of $T_{e,\mathrm{sep,OMP}}$ with $n_{e,\mathrm{sep,OMP}}$ in experiment compared to simulation, then this inferred $n_{e,\mathrm{sep,OMP}}$ would have a larger range than the actual $n_{e,\mathrm{sep,OMP}}$, resulting in a stronger decrease in the integrated measured $\Gamma_{\perp t}$ as a function of the actual $n_{e,\mathrm{sep,OMP}}$.

[43] Including the target fluxes plotted in figure 8(and the factor 1.8 shown there), the peak heat loads in figure 9, and the Fulcher front sensitivity shown in figure 12.

[44] Equivalent fuelling scans were simulated with drift terms turned off for the default CD and SXD fuelling scans. As expected (at least in the absence of the kind of instabilities considered in [56]), the up-down power ratio for those cases was symmetric (within a 3% margin).

[45] Defined to increase clockwise and to be zero at the lower inner target. Poloidal fluxes are positive in the direction of increasing poloidal distance.

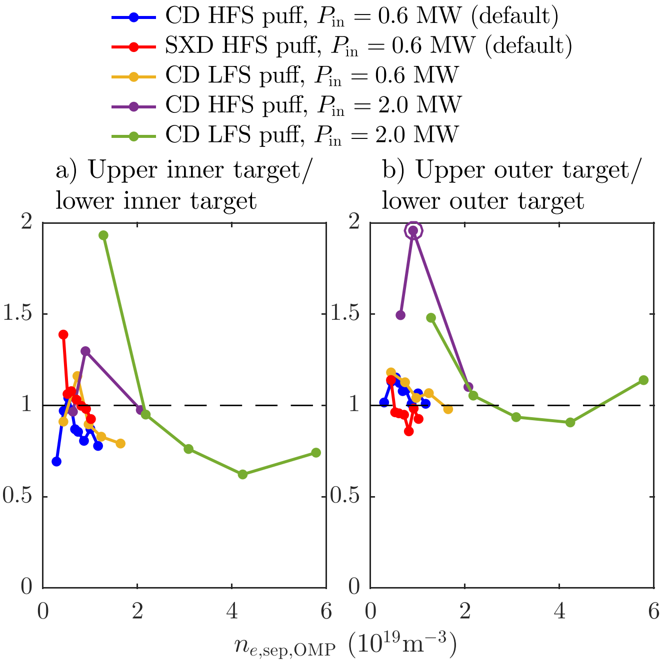

Figure 19. Up-down integrated target power asymmetries for (*a*) the inner targets and (*b*) the outer targets, for the default CD and SXD simulations, as well as the higher powered CD simulations, as labelled.

respectively. The poloidal plasma energy flux density is given by[46]

$$\begin{aligned} Q_{x,\text{plasma}} = & \frac{5}{2} n b_x V_{\parallel} (T_e + T_i) - b_x \frac{j_{\parallel}}{e} T_e \left(\frac{5}{2} + 0.71 \right) \\ & - b_x \left(\kappa_{e\parallel} \frac{\partial T_e}{\partial s} + \kappa_{i\parallel} \frac{\partial T_i}{\partial s} \right) \\ & + \frac{5}{2} n b_z V_{\perp}^{(E\times B)} (T_e + T_i) \\ & + \frac{5}{2} n b_z V_{\perp}^{(\nabla B)} \left(T_i - T_e^2 / T_i \right) + \frac{5}{2} n b_z V_{\perp}^{(\text{in})} T_i \\ & + \frac{5}{2} n b_z V_{\perp}^{(\text{vis})} T_i + \Gamma_{ix} \left(\frac{1}{2} m_i V_{\parallel}^2 + 13.6\text{eV} \right), \quad (13) \end{aligned}$$

where $b_x = B_x/B$, $b_z = B_z/B$ ('x' is the poloidal direction and 'z' is the toroidal direction) and '$\perp$' denotes the binormal direction (perpendicular to both the magnetic field and the radial direction). $V_{\parallel}$ is the parallel ion velocity and $j_{\parallel}$ is the parallel current. The poloidal ion flux density is given by

$$\Gamma_{ix} = n b_x V_{\parallel} + n b_z \left(V_{\perp}^{(E\times B)} + V_{\perp}^{(\nabla B)} + V_{\perp}^{(\text{in})} + V_{\perp}^{(\text{vis})} \right), \quad (14)$$

where $V_{\perp}^{(E\times B)}$, $V_{\perp}^{(\nabla B)}$, $V_{\perp}^{(\text{in})}$ and $V_{\perp}^{(\text{vis})}$ are the binormal drift velocities due to $E \times B$, ∇B, inertia and viscosity, respectively, and are given in [19] ($V_{\perp}^{(\nabla B)}$ is labelled as $\tilde{V}_{\perp}^{(\text{dia})}$ in that paper). For the simulation plotted in figure 20, only the first 5 terms in (13) are non-negligible, and are plotted in figures 20(*a*) and (*e*). The first term is the component of $Q_{x,\text{plasma}}$ convected by the parallel ion flow. The second term is electron convection associated with parallel current and the third is the component due to parallel heat conduction. The fourth and fifth terms are the components due to the binormal $E \times B$ drift (same direction electrons and ions) and the ∇B drift (opposite direction for electrons and ions; note that this makes no direct contribution to the energy flux when $T_e = T_i$)[47].

We see from figure 20(*a*) that the up-down power asymmetry on the HFS is associated primarily with a poloidal $E \times B$ drift (blue) and a parallel current (purple), both of which act to load the upper inner target[48]. This is similar to the situation depicted in figure 4 of [57] where, for the HFS, the thermoelectric current (from hotter upper inner target to cooler lower inner target) enhances the up-down asymmetry driven by the poloidal $E \times B$ flow. The picture is qualitatively different from [57] on the LFS, however. In figure 20(*e*) we see that the poloidal $E \times B$ energy flux (blue) is indeed towards the lower outer target as expected for a radially positive electric field (and depicted in [57]), but the energy it conveys is outweighed by the energy fluxes due to parallel ion convection (yellow) and $j_{\parallel}$ (purple, i.e. the first and second terms in (13), respectively). These both push energy to the *upper* outer target.

To understand the origin of the parallel ion flow, consider the radial[49] flux densities of ion particles across the LFS separatrix, shown in figure 20(*d*). These are dominated by $E \times B$ and ∇B drifts, as well as anomalous diffusion, as labelled[50]. Between the two X-points on the LFS, the radial ∇B drift (red) is the dominant component of the radial ion flux, removing ions from the upper LFS SOL and pushing them into the lower LFS SOL (see also the schematic in figure 20(*c*). This sets up a parallel return flow (and a corresponding parallel current) towards the upper outer target; a so-called Pfirsch-Schlüter flow/current (see section 18.5 of [36]). In the absence of any other currents or particle sources, one would expect the resulting convective cell to be closed and so not drive up-down asymmetries. However, one must also consider the presence of an additional parallel thermoelectric (positive) current towards the lower outer target, driven by an increased

---

[46] For simplicity we give the case for a pure deuterium plasma here. This is accurate for our simulations where carbon made a negligible contribution to the plasma energy flux.

[47] The inertial and viscous drift velocities are negligible for electrons so are only multiplied by T_i. The last term is the component due to convection of the kinetic energy of the ion flow and the potential of electrons to recombine with ions. At high density, this term can become dominant at the target and its reduction can only be achieved via the reduction in Γ_{ix} associated with detachment.

[48] Note that in figure 20(*c*) the $j_{\parallel}$ arrows point in the direction of positive current, which is opposite to the direction of the associated energy flow (recall the negative sign in front of the $j_{\parallel}$ term in (13)).

[49] Perpendicular to flux surfaces, positive in the direction of increasing poloidal magnetic flux.

[50] Note that, at the HFS mid-plane, there is a strong anomalous diffusion *into* the core (figure 20(*b*)). This is due to density peaking in the HFS SOL, driven by ionisation of the HFS puff. Furthermore, in addition to the radial ∇B drifts, there are also radial $E \times B$ drifts across the X-points, which transport particles from the lower LFS SOL to the lower HFS SOL, and from the upper HFS SOL to the upper LFS SOL. These are seen as peaks of opposite sign around the X-points in figures 20(*b*) and (*d*). The corresponding parallel return flow opposes the return flow driven by the ∇B drifts, but is relatively small in this case.

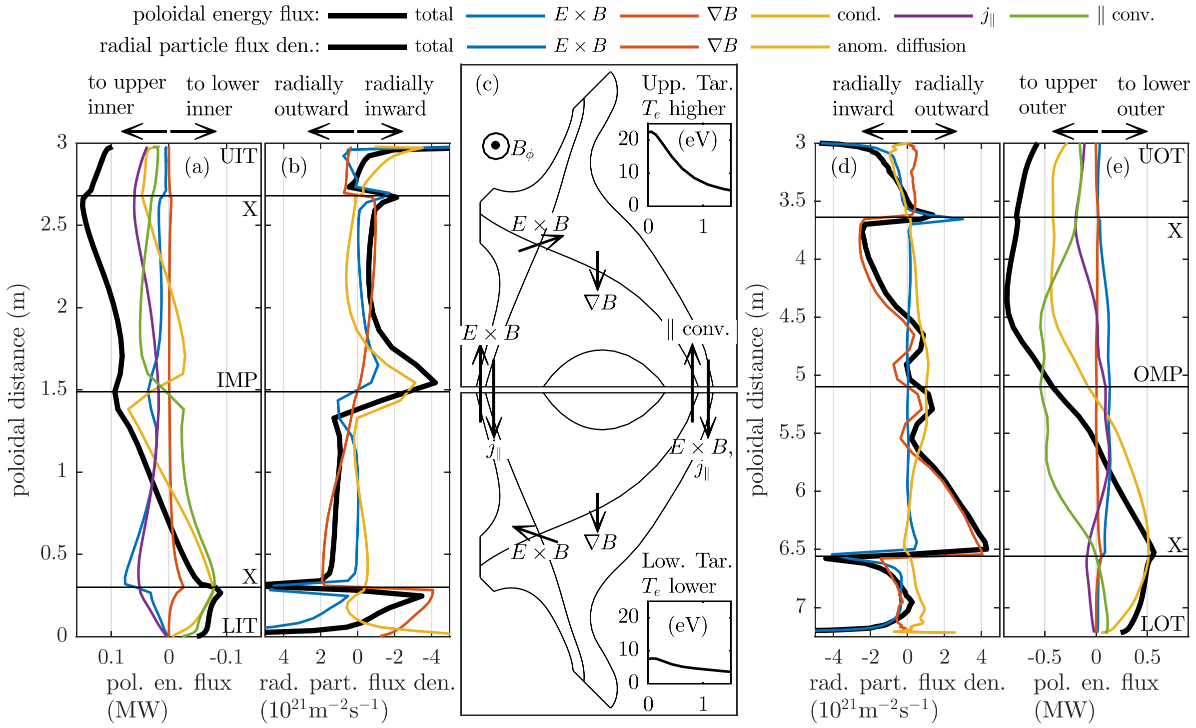

Figure 20. The mechanisms by which drift and current terms can drive power to both the upper targets in a connected double null, for the case where the ion ∇B drift points downwards. Plots are made for the $P_{\text{in}} = 2.0$ (HFS puff) simulation with the highest outer up-down asymmetry, highlighted with a purple open circle in figure 19(*b*). (*a*), (*e*) The total plasma poloidal energy flux (radially integrated over the entire SOL) as a function of poloidal distance, with components as labelled, in (*a*) the HFS SOL and (*e*) the LFS SOL. (*b*), (*d*) The total ion radial particle flux density crossing (*b*) the HFS separatrix and (*d*) the LFS separatrix, with components as labelled. (*c*) The important drift and current directions are shown schematically. Outer target T_e profiles (as a function of $R - R_{\text{sep,OMP}}$ in cm) are also inset.

T_e at the upper outer target compared to the lower outer target (the steady-state outer target T_e profiles are shown inset in figure 20(*c*). This parallel thermoelectric current is carried by a parallel convection of electrons to the *upper* outer target and acts to preferentially load it. In addition, its presence requires that the aforementioned convective cell must now be lopsided (i.e. fewer ions are removed from the upper LFS SOL by the ∇B drift than are pushed into the lower LFS SOL, figure 20(*d*), in order to maintain $\nabla.\vec{j} = 0$. As a result, a significant portion of the power conveyed by the Pfirsch-Schlüter parallel ion flow towards the upper outer target remains beyond the upper X-point, preferentially loading the upper outer target.

This apparent synergy between the thermoelectric current and the Pfirsch-Schlüter flow is difficult to fully assess from a single converged solution. Future studies in which the simulation targets are set to the floating potential, forcing the net current to the targets to zero, may offer further insight. Given the competing mechanisms outlined above ($E \times B$ vs. parallel thermoelectric currents and parallel Pfirsch-Schlüter ion flows), it seems unlikely that there is a general up-down asymmetry direction for all connected double null plasmas.

In figure 19 it was shown that at higher density, the LFS up-down asymmetry is reduced. This appears to be due to a combination of reduced thermoelectric parallel currents in the SOL (due to a reduced difference in target temperatures), combined with the fact that, at higher density, particle sources due to radial anomalous transport across the separatrix and ionisation in the divertor start to dominate, reducing the impact of the Pfirsch-Schlüter flow. In conclusion, there are clearly several competing mechanisms which can drive up-down asymmetries in either direction, but in general the asymmetries appear to increase with decreasing collisionality.

6. Conclusions

We draw the following conclusions from this work:

- At comparable upstream separatrix densities ($\approx 7 \times 10^{18}$ m^{-3}), IR heat load measurements of MAST-U ohmic L-mode plasmas suggest a significant reduction in the peak heat load in SXD compared to CD, with minimal effect on the upstream n_e and T_e profiles. Due to uncertainties in the IR measurements, the experimentally-inferred reduction factor of 16 ± 7 also has a large uncertainty. However, interpretative SOLPS-ITER simulations calculate it to be 27, suggesting the experimental value to be towards the upper end of the quoted range.
- Of that factor 27 reduction in the simulations, a factor 2.9 is due to additional dissipation mechanisms in the SXD, which occur downstream of the CD target, due to a net radial transport of atom energy away from the critical flux tube. Our

analysis emphasises the critical importance of the extended leg in providing space behind the $T_e = 5$ eV location, for neutrals to transport energy radially away from the flux tube where the target energy flux density is maximum. Further factors of 4.9 and 1.9 are due to poloidal and toroidal flux expansion, respectively.

- Carbon radiation is found to be a negligible sink of power in the lower outer divertor in the simulations. The slight overestimate of the emissivity from C^{2+} ions in the simulations compared to experiment suggests that carbon radiation is also negligible in the lower outer divertor in experiment, in line with recent experimental power balance measurements [55].
- Large (factor $\gtrsim 3$) reductions in $T_{e,\mathrm{sep,OMP}}$ are observed with increasing edge density, in both simulations and experiment (assuming a fixed offset in the EFIT-derived separatrix position). These reductions are driven by a transition towards a convection-dominated regime at high density, combined with a transition to the sheath limited regime and stronger flux limiting at low density. Understanding this effect is an important part of interpreting the presented data, but is only expected in low powered, neutrally transparent plasmas.
- In experiment, there is only a small upstream density window in which CD and SXD configurations overlap without strike point splitting (thought to be the result of error field penetration at low density). Scenario development is underway to widen this window of overlap and to push the SXD into attached regimes. Both of those goals may require higher powered H-mode plasmas which, although more reactor relevant, are also less easily interpreted due to ELM transients.
- This strike point splitting makes it difficult to draw strong conclusions on the target ion flux rollover with increasing $n_{e,\mathrm{sep,OMP}}$. Even so, simulated values for the near separatrix $\Gamma_{\perp t}$ at the outer targets do fall within the experimental scatter. Those simulations calculate a factor 1.8 increase in the required $n_{e,\mathrm{sep,OMP}}$ for rollover in CD compared to SXD, in line with simple two-point model arguments.
- However, after rollover, the reduction in the target integrated $\Gamma_{\perp t}$ at the upper outer target is not reproduced by the simulations. Indeed, by this measure, the CD simulations fail to rollover at all while the SXD simulations underestimate the integrated $\Gamma_{\perp t}$ after rollover (and the reduction that is observed in the SXD simulations can be largely attributed to the narrower numerical grid in that configuration). One possible reason for this is a potential underestimate of the molecular charge exchange cross sections in the default neutral model used here, resulting in an underestimate of the reduction in target flux due to MAR [41–43]. Future work will include an assessment of the sensitivity of the simulated post-rollover reduction in $\Gamma_{\perp t}$ to the molecular charge exchange rate, which has recently been shown to significantly strengthen the target flux reduction on TCV [43].
- In the CD configuration, another explanation for the strong rollover observed in experiment is an unstable collapse in the upstream separatrix pressure, brought about by large neutral power losses from the core, due to strong gas fuelling at high density. Mid-plane pressure profiles and bolometry measurements support this hypothesis and, beyond a critical upstream density in the simulations, an unstable collapse in $\Gamma_{\perp t}$ is also simulated, with concomitant drops in upstream pressure and increases in core neutral losses. In CD simulations, the $n_{e,\mathrm{sep,OMP}}$ at which this collapse occurs can be increased by switching the D_2 fuelling location to the LFS, or by increasing the input power from 0.6 MW to 2.0 MW, but *both* of these modifications are required to achieve a stable rollover driven by electron-ion volume recombination in the divertor.
- Spectral observations in the SXD lower outer divertor show line emission generally moving off and away from the target with increasing $n_{e,\mathrm{sep,OMP}}$. In simulation, the Fulcher fronts (where the Fulcher emissivity drops to some fraction of it is maximum) correlate well with isothermal contours. The Fulcher fronts pull away from the target at similar $n_{e,\mathrm{sep,OMP}}$ in both simulation and experiment, and that $n_{e,\mathrm{sep,OMP}}$ corresponds to the value at which the simulated near separatrix $\Gamma_{\perp t}$ rolls over. The subsequent sensitivity of the Fulcher front positions to further increases in $n_{e,\mathrm{sep,OMP}}$ also agrees well between simulation and experiment.
- Parallel gradients in the magnetic field strength act to stabilise the parallel detachment front position against changes in $n_{e,\mathrm{sep,OMP}}$, in qualitative agreement with simple models [8, 9]. Poloidal B-field gradients also appear to stabilise the poloidal front position. However, in the SXD geometry considered here, the change in $L_{\nabla_x B}$ was much weaker than the change in $L_{\nabla_{\parallel} B}$, making the effect in poloidal space less pronounced. For a reactor, this work motivates the consideration of high B-field gradients in regions along the leg where improved stabilisation of the detachment front is desirable (for control or heat buffering purposes).
- The role of drifts in the simulations is generally small for $P_{\mathrm{in}} = 0.6$ MW. However, for $P_{\mathrm{in}} = 2.0$ MW there can be significant up-down asymmetries in the simulations at low $n_{e,\mathrm{sep,OMP}}$, with up to twice the power going to the upper outer target compared to the lower outer. On the LFS in the standard MAST-U magnetic configuration (∇B drift down), the parallel Pfirsch-Schlüter flow towards the upper outer divertor combines with a thermoelectric current convecting electrons to the upper outer target. For the cases studied, these overcome the poloidal $E \times B$ flow towards the lower outer divertor. However, this delicate balance of competing effects means that the exact up-down balance in connected double null should be considered on a case by case basis.

Acknowledgments

This work has been funded by the EPSRC Energy Programme [Grant Number EP/W006839/1]. To obtain further information on the data and models underlying this paper please contact PublicationsManager@ukaea.uk.

Appendix A. Simulation catalog

Table A1 lists the converged SOLPS-ITER simulations presented in this paper. These were catalogued using the

Table A1. The catalogued SOLPS-ITER simulations used in this paper. Simulations can be accessed at the web address corresponding to their alias, with the prefix 'https://simdb.ukaea.uk/alias/dmoulton/solps-iter/mastu/' (access for non UKAEA staff can be granted on request). 'HFSMP' and 'LFSMP' stand for 'high field side mid-plane' and 'low field side mid-plane', respectively. Aliases in bold comprise the reference fuelling scans in CD and SXD; those with asterisks correspond to the 'CD-LD', 'CD-MD', 'CD-HD', 'SXD-LD', 'SXD-MD' and 'SXD-HD' cases.

Config.	Input power (MW)	D$_2$ puff rate (10^{21}el. s^{-1})	D$_2$ puff location	Wall recycling coefficient	Reduced PFR transport?	Drifts?	SimDB alias
CD	0.6	1.0	HFSMP	0.999	Yes	Yes	**45 470/Dec1623/seq-1***
CD	0.6	2.0	HFSMP	0.999	Yes	Yes	**45 470/Dec1623/seq-2**
CD	0.6	3.0	HFSMP	0.999	Yes	Yes	**45 470/Dec1623/seq-3**
CD	0.6	4.0	HFSMP	0.999	Yes	Yes	**45 470/Dec1623/seq-4**
CD	0.6	5.0	HFSMP	0.999	Yes	Yes	**45 470/Dec1623/seq-5***
CD	0.6	6.0	HFSMP	0.999	Yes	Yes	**45 470/Dec1623/seq-6**
CD	0.6	8.0	HFSMP	0.999	Yes	Yes	**45 470/Dec1623/seq-7**
CD	0.6	10.0	HFSMP	0.999	Yes	Yes	**45 470/Dec1623/seq-8**
CD	0.6	12.0	HFSMP	0.999	Yes	Yes	**45 470/Dec1623/seq-9***
CD	0.6	2.0	LFSMP	0.999	Yes	Yes	45 470/Dec1623/seq-10
CD	0.6	6.0	LFSMP	0.999	Yes	Yes	45 470/Dec1623/seq-11
CD	0.6	10.0	LFSMP	0.999	Yes	Yes	45 470/Dec1623/seq-12
CD	0.6	14.0	LFSMP	0.999	Yes	Yes	45 470/Dec1623/seq-13
CD	0.6	18.0	LFSMP	0.999	Yes	Yes	45 470/Dec1623/seq-14
CD	0.6	0.6	HFSMP	0.9999	Yes	Yes	45 470/Dec1623/seq-15
CD	0.6	1.0	HFSMP	0.9999	Yes	Yes	45 470/Dec1623/seq-16
CD	0.6	2.0	HFSMP	0.9999	Yes	Yes	45 470/Dec1623/seq-17
CD	0.6	3.0	HFSMP	0.9999	Yes	Yes	45 470/Dec1623/seq-18
CD	0.6	4.0	HFSMP	0.9999	Yes	Yes	45 470/Dec1623/seq-19
CD	0.6	5.0	HFSMP	0.9999	Yes	Yes	45 470/Dec1623/seq-20
CD	0.6	6.0	HFSMP	0.9999	Yes	Yes	45 470/Dec1623/seq-21
CD	0.6	1.0	HFSMP	0.999	No	Yes	45 470/Dec1623/seq-22
CD	0.6	2.0	HFSMP	0.999	No	Yes	45 470/Dec1623/seq-23
CD	0.6	3.0	HFSMP	0.999	No	Yes	45 470/Dec1623/seq-24
CD	0.6	4.0	HFSMP	0.999	No	Yes	45 470/Dec1623/seq-25
CD	0.6	5.0	HFSMP	0.999	No	Yes	45 470/Dec1623/seq-26
CD	0.6	6.0	HFSMP	0.999	No	Yes	45 470/Dec1623/seq-27
CD	0.6	8.0	HFSMP	0.999	No	Yes	45 470/Dec1623/seq-28
CD	0.6	10.0	HFSMP	0.999	No	Yes	45 470/Dec1623/seq-29
CD	0.6	12.0	HFSMP	0.999	No	Yes	45 470/Dec1623/seq-30
CD	0.6	0.5	HFSMP	0.999	Yes	No	45 470/Dec1623/seq-31
CD	0.6	1.0	HFSMP	0.999	Yes	No	45 470/Dec1623/seq-32
CD	0.6	2.0	HFSMP	0.999	Yes	No	45 470/Dec1623/seq-33
CD	0.6	3.0	HFSMP	0.999	Yes	No	45 470/Dec1623/seq-34
CD	0.6	4.0	HFSMP	0.999	Yes	No	45 470/Dec1623/seq-35
CD	0.6	5.0	HFSMP	0.999	Yes	No	45 470/Dec1623/seq-36
CD	0.6	6.0	HFSMP	0.999	Yes	No	45 470/Dec1723/seq-1
CD	0.6	7.0	HFSMP	0.999	Yes	No	45 470/Dec1723/seq-2
CD	0.6	8.0	HFSMP	0.999	Yes	No	45 470/Dec1723/seq-3
CD	0.6	10.0	HFSMP	0.999	Yes	No	45 470/Dec1723/seq-4
CD	0.6	12.0	HFSMP	0.999	Yes	No	45 470/Dec1723/seq-5
CD	2.0	5.0	HFSMP	0.999	Yes	Yes	45 470/Dec1723/seq-6
CD	2.0	10.0	HFSMP	0.999	Yes	Yes	45 470/Dec1723/seq-7
CD	2.0	40.0	HFSMP	0.999	Yes	Yes	45 470/Dec1723/seq-8
CD	2.0	20.0	LFSMP	0.999	Yes	Yes	45 470/Dec1723/seq-9
CD	2.0	50.0	LFSMP	0.999	Yes	Yes	45 470/Dec1723/seq-10
CD	2.0	80.0	LFSMP	0.999	Yes	Yes	45 470/Dec1723/seq-11
CD	2.0	110.0	LFSMP	0.999	Yes	Yes	45 470/Dec1723/seq-12
CD	2.0	140.0	LFSMP	0.999	Yes	Yes	45 470/Dec1723/seq-13

(Continued.)

Table A1. (Continued.)

SXD	0.6	0.2	HFSMP	0.999	Yes	No	**45 456/Dec1523/seq-4**
SXD	0.6	0.5	HFSMP	0.999	Yes	No	**45 456/Dec1523/seq-5***
SXD	0.6	1.0	HFSMP	0.999	Yes	No	**45 456/Dec1523/seq-6**
SXD	0.6	1.6	HFSMP	0.999	Yes	Yes	**45 456/Dec1523/seq-7**
SXD	0.6	2.3	HFSMP	0.999	Yes	Yes	**45 456/Dec1523/seq-8***
SXD	0.6	3.0	HFSMP	0.999	Yes	Yes	**45 456/Dec1523/seq-9**
SXD	0.6	4.0	HFSMP	0.999	Yes	Yes	**45 456/Dec1523/seq-10***
SXD	0.6	5.0	HFSMP	0.999	Yes	Yes	**45 456/Dec1523/seq-11**
SXD	0.6	6.0	HFSMP	0.999	Yes	Yes	**45 456/Dec1523/seq-12**
SXD	0.6	7.0	HFSMP	0.999	Yes	Yes	**45 456/Dec1523/seq-13**
SXD	0.6	1.0	HFSMP	0.999	No	Yes	45 456/Dec1523/seq-14
SXD	0.6	1.2	HFSMP	0.999	No	Yes	45 456/Dec1523/seq-15
SXD	0.6	1.3	HFSMP	0.999	No	Yes	45 456/Dec1523/seq-16
SXD	0.6	1.6	HFSMP	0.999	No	Yes	45 456/Dec1523/seq-17
SXD	0.6	2.3	HFSMP	0.999	No	Yes	45 456/Dec1523/seq-18
SXD	0.6	3.0	HFSMP	0.999	No	Yes	45 456/Dec1523/seq-19
SXD	0.6	4.0	HFSMP	0.999	No	Yes	45 456/Dec1523/seq-20
SXD	0.6	5.0	HFSMP	0.999	No	Yes	45 456/Dec1523/seq-21
SXD	0.6	6.0	HFSMP	0.999	No	Yes	45 456/Dec1523/seq-22
SXD	0.6	1.5	HFSMP	0.999	Yes	No	45 456/Dec1523/seq-23
SXD	0.6	2.0	HFSMP	0.999	Yes	No	45 456/Dec1523/seq-24
SXD	0.6	3.0	HFSMP	0.999	Yes	No	45 456/Dec1523/seq-25
SXD	0.6	4.0	HFSMP	0.999	Yes	No	45 456/Dec1523/seq-26
SXD	0.6	5.0	HFSMP	0.999	Yes	No	45 456/Dec1523/seq-27
SXD	0.6	6.0	HFSMP	0.999	Yes	No	45 456/Dec1523/seq-28

SimDB simulation database management system [58] and contain all necessary input and output files for analysing and rerunning the simulations.

Appendix B. Target profile comparisons; motivating reduced transport in the outer PFR

B.1. Conventional configuration

Figure B1 compares the target ion flux and heat load profiles for the CD, and serves to motivate the reduced transport applied to the outer PFR region in the default simulations presented in this paper. The small dots in figures B1(*a*)–(*f*) show the probe-measured upper (*a*)–(*c*) and lower (*d*)–(*f*) outer target $\Gamma_{\perp t}$. There was some missing coverage at the lower outer target in the region 3 cm$\lesssim R_t - R_{\mathrm{sep},t} \lesssim$8 cm, but the peak $\Gamma_{\perp t}$ is still resolved. In figures B1(*g*)–(*i*), the dots show the IR-measured heat flux density normal to the target surface, $Q_{\perp t}$ (also referred to as the heat load). Our analysis of the measured, toroidally-resolved heat load suggests that the toroidally shadowed region accounts for $\lesssim$10% of the 2π radians around the machine, allowing us to directly compare the measured heat load at a fixed toroidal location to the toroidally symmetric SOLPS-ITER calculation (at least for cases without strike point splitting). All profiles in figure B1 are plotted as a function of the major radial distance past the EFIT-calculated separatrix, at the target.

A subset of the data (within 3.5×10^{17} m^{-3} of the simulated $n_{e,\mathrm{sep,OMP}}$ for the probes or within 1×10^{17} m^{-3} of the simulated $n_{e,\mathrm{sep,OMP}}$ for the more frequent IR measurements) was picked out for comparison to each of the three simulations CD-LD, CD-MD and CD-HD. With the exception of shot 45 469 (the only Conventional shot without strike point splitting, plotted in orange), all of the experimental data in figure B1 has been plotted in grey. This is to emphasise our lack of confidence when comparing a toroidally symmetric SOLPS-ITER simulation to a toroidally asymmetric experiment with strike point splitting. Quantifying the uncertainties involved in such a comparison is beyond the scope of this work; the reader is therefore advised to focus primarily on the comparison between SOLPS-ITER simulations and the orange dots in figure B1.

In figures B1(*a*)–(*f*), the $\Gamma_{\perp t}$ profiles are shown in green for the default simulations (with a factor 20 reduction in the outer PFR anomalous transport) and in magenta for equivalent simulations without any reduction in the PFR anomalous transport. The agreement with experiment is significantly improved with the reduced PFR transport, both in the outer PFR fall off length and the peak $\Gamma_{\perp t}$ value. It is based on this improvement that we have selected the reduced outer PFR transport simulations as our default set. For consistency, we applied the same reduction to the default SXD simulations (although, as shown in figure B2, the effect is less pronounced in SXD). A reduction in the outer PFR anomalous transport is consistent with strong

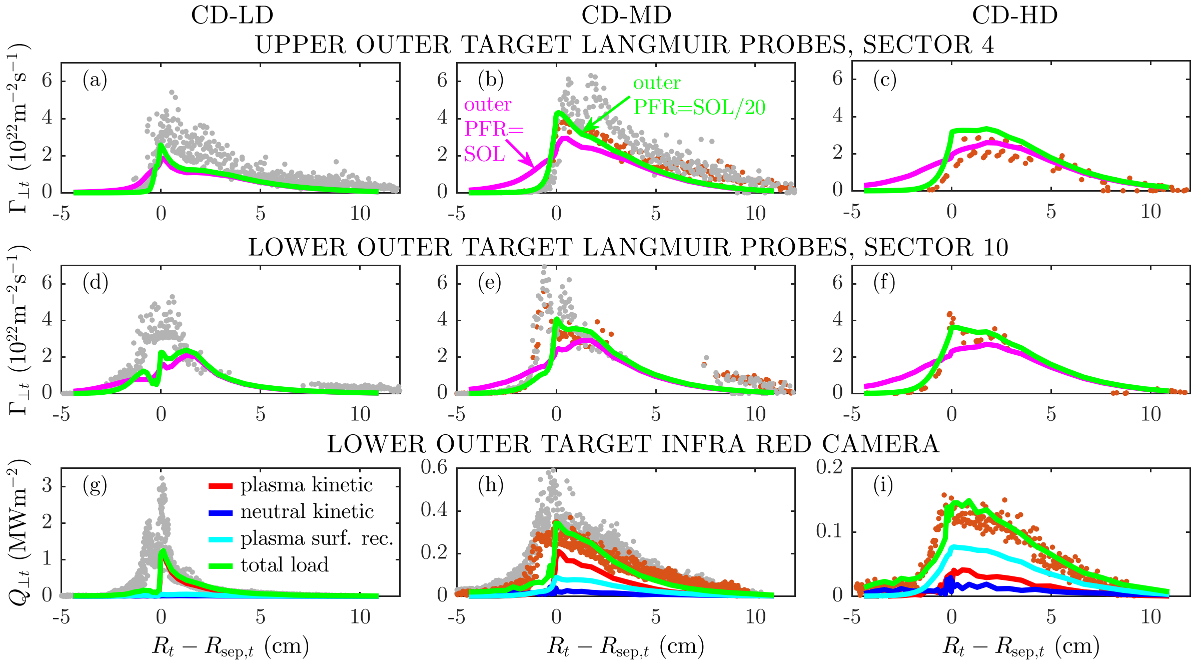

Figure B1. Target profiles in simulation (solid lines) and experiment (dots), in the Conventional configuration. Grey dots indicate shots with strike point splitting, orange dots are from shot 45469 (without splitting). (*a*)–(*c*) Upper and (*d*)–(*f*) lower outer target ion particle flux density normal to a toroidally symmetric target surface. Experimental measurements are from Langmuir probes. Magenta lines show simulations with equal anomalous transport in the PFR and SOL. Green lines show the default simulations, in which the outer PFR anomalous transport was reduced by a factor 20. (*g*)–(*i*) Heat loads on the lower outer target (inferred experimentally from the infra-red camera). The simulated heat loads (for the default PFR-reduced-transport cases) are shown in green, alongside their main components as labelled in (*g*).

shearing in the outer PFR of filaments born in the inner PFR, as previously reported on MAST [59, 60].

In figures B1(*g*) and (*h*), the total simulated loads are shown in green. The components are also shown, due to the kinetic energy of plasma particles (red), the kinetic energy of the neutral particles (blue), and the potential energy released when ions and electrons recombine in the target substrate (cyan). The loads due to radiation and due to atoms combining into molecules in the substrate were found to be negligible. As $n_{e,\mathrm{sep,OMP}}$ increases, the peak total heat load reduces by a factor 8.3, from 1.2 MWm^{-2} in CD-LD to 0.15 MWm^{-2} in CD-HD (note the reduction in *y*-axis limits from figure B1(*g*) and (*h*)). Concomitant with this reduction, the load becomes increasingly due to surface plasma recombination and decreasingly due to the kinetic energy of the plasma.

B.2. Super-X configuration

Figure B2 repeats the comparison between simulated and measured target profiles for the Super-X configuration. Only the highest density shots (45 463 in red and 45 464 in pink) avoided strike point splitting. In this case, therefore, we can only compare experimental data to the SXD-HD simulation with confidence, although comparisons for SXD-LD and SXD-MD are provided for completeness (with the experimental data in grey).

For $\Gamma_{\perp t}$, the agreement with the SXD-HD simulation is reasonable, although the simulation shows a SOL broadening at the upper outer target which was not observed experimentally. In Super-X, $\Gamma_{\perp t}$ data was also available from sector 10 for the upper outer target. There is some discrepancy (factor $\lesssim 2$) between the two sectors, the origin of which is still under investigation. For the shots without strike point splitting, there is no evidence of experimental up-down asymmetries beyond the measured variation in $\Gamma_{\perp t}$. The simulations do exhibit some up-down asymmetry, particularly in the peak and PFR, with a broader PFR profile at the lower outer target. However, probe data was not available in the lower outer target PFR to verify this experimentally.

As for the CD-HD simulation (figure B1(*i*)), the total load in the SXD-HD simulation is dominated by plasma surface recombination. The difference with CD-HD is that the simulation is now so strongly detached that neutral kinetic loads dominate over the plasma kinetic load.

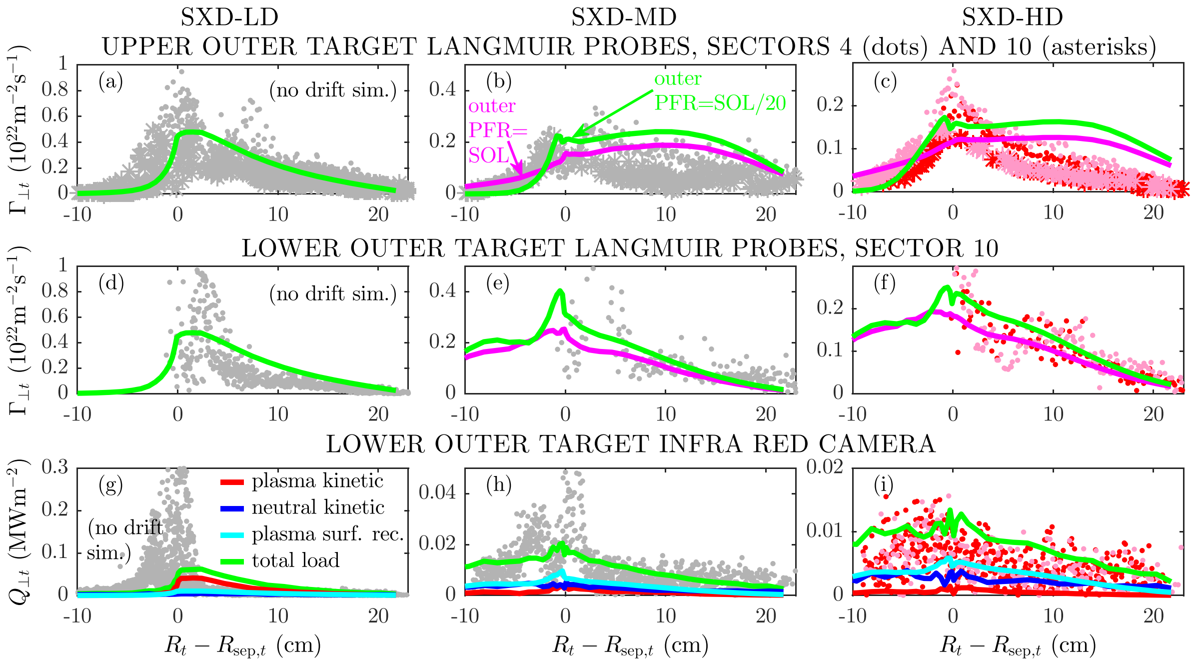

Figure B2. Target profiles in simulation (solid lines) and experiment (dots), in the Super-X configuration. As figure B2 but for the Super-X. Red and pink dots are from shot 45463 and 45464, respectively, and do not exhibit strike point splitting. Additional probe data from toroidal sector 10 for the upper outer target is shown as asterisks. Note that the SXD-LD simulation has drifts turned off, as indicated.

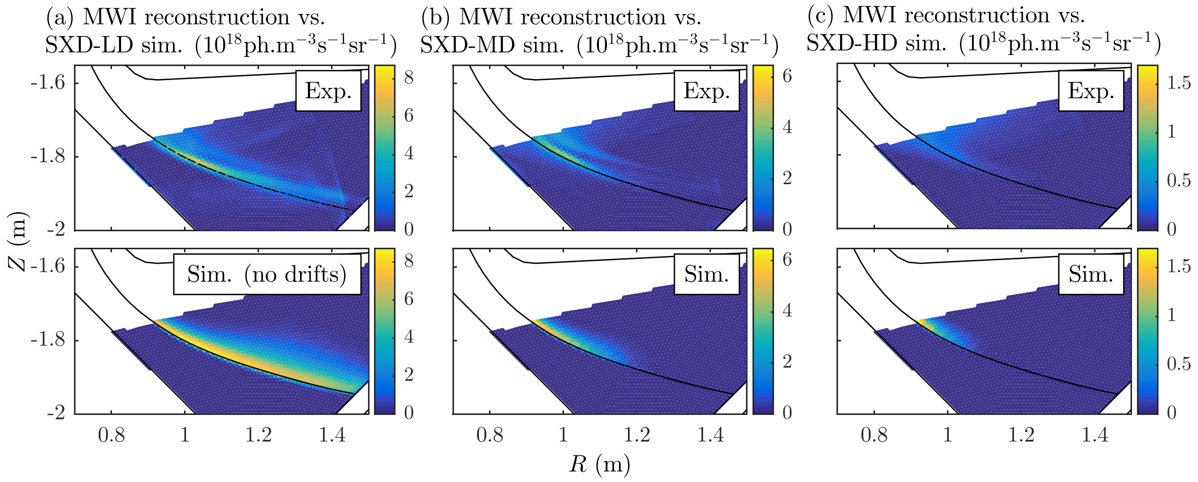

Figure C1. Comparison between the CIII (465 nm) emissivity in simulation and experiment, for the SXD-LD, SXD-MD and SXD-HD simulations, following the same formatting as figures 10(*a*)–(*c*).

Appendix C. Carbon radiation comparisons

Figure C1 repeats figures 10 and 12 for the MWI comparison between simulation and experiment, but now with the CIII (465 nm) filter applied (due to emission from C^{2+} ions). Similar to the Dα and Fulcher emission, there is reasonable agreement in the location of the emission for the SXD-LD and SXD-MD cases, whilst for the SXD-HD case the simulation underestimates the degree to which the emission moves away from the target. Importantly, the absolute emissivity calculated by the code is ~50% *higher* in simulation compared to experiment. Since carbon radiation is a negligible power sink in the simulations (section 5.2), this implies that carbon radiation is also negligible in experiment, at least in the lower outer divertor. These findings are in line with recent experimental calculations which also infer a negligible contribution from carbon radiation in the lower outer divertor [55].

ORCID iDs

J.R. Harrison https://orcid.org/0000-0003-2906-5097
L. Xiang https://orcid.org/0000-0001-8175-6640
K. Verhaegh https://orcid.org/0000-0002-0500-2764
T.A. Wijkamp https://orcid.org/0000-0003-3110-8682
F. Federici https://orcid.org/0000-0002-9354-7309
B. Lipschultz https://orcid.org/0000-0001-5968-3684

References

[1] Morris A.W. 2012 MAST: results and upgrade activities *IEEE Trans. Plasma Sci.* **40** 682

[2] Harrison J.R. *et al* 2019 Overview of new MAST physics in anticipation of first results from MAST Upgrade *Nucl. Fusion* **59** 112011

[3] Valanju P.M., Kotschenreuther M., Mahajan S. and Canik J. 2009 Super-X divertors and high power density fusion devices *Phys. Plasmas* **16** 056110

[4] Kotschenreuther M., Valanju P., Wiley J., Rognlein T., Mahajan S. and Pekker M. 2004 Scrape off layer physics for burning plasmas and innovative divertor solutions *Proc. 20th IAEA Int. Conf in Fusion Energy* (*Vilamoura, Portugal*)

[5] Xiang L., Militello F., Moulton D., Subba F., Aho-Mantila L., Coster D., Wensing M., Lunt T., Wischmeier M. and Reimerdes H. 2021 The operational space for divertor power exhaust in DEMO with a super-X divertor *Nucl. Fusion* **61** 076007

[6] Wiesen S. *et al* 2015 The new SOLPS-ITER code package *J. Nucl. Mater.* **463** 480

[7] Bonnin X., Dekeyser W., Pitts R., Coster D., Voskoboynikov S. and Wiesen S. 2016 Presentation of the new SOLPS-ITER code package for tokamak plasma edge modelling *Plasma Fusion Res.* **11** 1403102

[8] Lipschultz B., Parra F.I. and Hutchinson I.H. 2016 Sensitivity of detachment extent to magnetic configuration and external parameters *Nucl. Fusion* **56** 056007

[9] Cowley C., Lipschultz B., Moulton D. and Dudson B. 2022 Optimizing detachment control using the magnetic configuration of divertors *Nucl. Fusion* **62** 086046

[10] Reinke M.L. 2017 Heat flux mitigation by impurity seeding in high-field tokamaks *Nucl. Fusion* **57** 034004

[11] Goldston R.J., Reinke M.L. and Schwartz J.A. 2017 A new scaling for divertor detachment *Plasma Phys. Control. Fusion* **59** 055015

[12] Pitts R.A. *et al* 2019 Physics basis for the first ITER tungsten divertor *Nucl. Mater. Energy* **20** 100696

[13] Moulton D., Harrison J., Lipschultz B. and Coster D. 2017 Using SOLPS to confirm the importance of total flux expansion in Super-X divertors *Plasma Phys. Control. Fusion* **59** 065011

[14] Theiler C. *et al* 2017 Results from recent detachment experiments in alternative divertor configurations on TCV *Nucl. Fusion* **57** 072008

[15] Fil A., Lipschultz B., Moulton D., Dudson B., Février O., Myatra O., Theiler C., Verhaegh K. and Wensing M. 2020 Separating the roles of magnetic topology and neutral trapping in modifying the detachment threshold for TCV *Plasma Phys. Control. Fusion* **62** 035008

[16] Fil A., Lipschultz B., Moulton D., Thornton A., Dudson B.D., Myatra O. and Verhaegh K. (the EUROfusion MST1 Team) 2022 Comparison between MAST-U conventional and Super-X configurations through SOLPS-ITER modelling *Nucl. Fusion* **62** 096026

[17] Carpita M. *et al* 2024 Parallel flows as a key component to interpret Super-X divertor experiments *Nucl. Fusion* **64** 046019

[18] Howell D., Hender T. and Cunningham G. 2007 Locked mode thresholds on the MAST spherical tokamak *Nucl. Fusion* **47** 1336

[19] Rozhansky V., Kaveeva E., Molchanov P., Veselova I., Voskoboynikov S., Coster D., Counsell G., Kirk A. and Lisgo S. 2009 New B2SOLPS5.2 transport code for H-mode regimes in tokamaks *Nucl. Fusion* **49** 025007

[20] Braginskii S.I. 1965 Transport processes in a plasma *Reviews of Plasma Physics* vol 1 (Consultants Bureau) p 205

[21] Reiter D. 2023 The EIRENE code user manual (available at: www.eirene.de/Documentation/eirene.pdf)

[22] Senichenkov I.Y., Kaveeva E.G., Sytova E.A., Rozhansky V.A., Voskoboynikov S.P., Veselova I.Y., Coster D.P., Bonnin X. and Reimold F. 2019 On mechanisms of impurity leakage and retention in the tokamak divertor *Plasma Phys. Control. Fusion* **61** 045013

[23] Marchand R. and Dumberry M. 1996 CARRE: a quasi-orthogonal mesh generator for 2D edge plasma modelling *Comput. Phys. Commun.* **96** 232

[24] Havlíčková E. *et al* 2015 SOLPS analysis of the MAST-U divertor with the effect of heating power and pumping on the access to detachment in the Super-x configuration *Plasma Phys. Control. Fusion* **57** 115001

[25] Kirk A. *et al* 2004 ELM characteristics in MAST *Plasma Phys. Control. Fusion* **46** 551

[26] De Temmerman G., Delchambre E., Dowling J., Kirk A., Lisgo S. and Tamain P. 2010 Thermographic study of heat load asymmetries during MAST L-mode discharges *Plasma Phys. Control. Fusion* **52** 095005

[27] Eckstein W. and Heifetz D.B. 1986 *Data Sets for Hydrogen Reflection and Their Use in Neutral Transport Calculations* (IPP Garching) p 9/59

[28] Bateman G. 1980 *Distribution of Neutrals Scattered off a Wall* (Princeton University Plasma Physics Lab) p 1

[29] García-Rosales C., Eckstein W. and Roth J. 1995 Revised formulae for sputtering data *J. Nucl. Mater.* **218** 8

[30] Roth J. *et al* 2004 Flux dependence of carbon chemical erosion by deuterium ions *Nucl. Fusion* **44** L21

[31] Huang J., Lisgo S. and Maddison G. (the MAST Team) 2010 Analysis of fuel retention on MAST by global gas balance *Plasma Phys. Control. Fusion* **52** 075012

[32] Fundamenski W. 2005 Parallel heat flux limits in the tokamak scrape-off layer *Plasma Phys. Control. Fusion* **47** R163

[33] Kaveeva E. *et al* 2020 SOLPS-ITER modelling of ITER edge plasma with drifts and currents *Nucl. Fusion* **60** 046019

[34] Cohen R.H. and Rognlien T.D. 1994 Finite mean-free-path effects in tokamak scrape-off layers *Contrib. Plasma Phys.* **34** 198

[35] Igitkhanov Y.L., Kukushkin A.S. and Runov A.M. 1994 Scrape off layer physics for burning plasmas and innovative divertor solutions *Proc. 21st EPS Conf. on Plasma Physics* (*Montpellier, France*) p 766

[36] Stangeby P.C. 2000 *The Plasma Boundary of Magnetic Fusion Devices* (Institute of Physics Publishing)

[37] Appel L.C. and Lupelli I. 2018 Equilibrium reconstruction in an iron core tokamak using a deterministic magnetisation model *Comput. Phys. Commun.* **223** 1

[38] Scannell R. *et al* 2008 Design of a new Nd:YAG Thomson scattering system for MAST *Rev. Sci. Instrum.* **79** 10E730

[39] Field A. *et al* 2004 The influence of gas fuelling location on H-mode access in the MAST spherical tokamak *Plasma Phys. Control. Fusion* **46** 981

[40] Ryan P.J., Elmore S.D., Harrison J.R., Lovell J. and Stephen R. 2023 Overview of the Langmuir probe system on the Mega Ampere Spherical Tokamak (MAST) Upgrade *Rev. Sci. Instrum.* **94** 103501

[41] Kukushkin A., Krasheninnikov S., Pshenov A. and Reiter D. 2017 Role of molecular effects in divertor plasma recombination *Nucl. Mater. Energy* **12** 984

[42] Verhaegh K. *et al* 2021 The role of plasma-molecule interactions on power and particle balance during detachment on the TCV tokamak *Nucl. Fusion* **61** 106014

[43] Verhaegh K. *et al* 2023 Investigating the impact of the molecular charge-exchange rate on detached SOLPS-ITER simulations *Nucl. Fusion* **63** 076015

[44] Petrie T. *et al* 2013 Effect of changes in separatrix magnetic geometry on divertor behaviour in DIII-D *Nucl. Fusion* **53** 113024

[45] Havlíčková E., Fundamenski W., Wischmeier M., Fishpool G. and Morris A. 2014 Investigation of conventional and Super-X divertor configurations of MAST Upgrade using scrape-off layer plasma simulation *Plasma Phys. Control. Fusion* **56** 075008

[46] Feng X. *et al* 2021 Development of an 11-channel multi wavelength imaging diagnostic for divertor plasmas in MAST Upgrade *Rev. Sci. Instrum.* **92** 063510

[47] Wijkamp T.A. *et al* 2023 Characterisation of detachment in the MAST-U Super-X divertor using multi-wavelength imaging of 2D atomic and molecular emission processes *Nucl. Fusion* **63** 056003

[48] Verhaegh K. *et al* 2023 Spectroscopic investigations of detachment on the MAST Upgrade Super-X divertor *Nucl. Fusion* **63** 016014

[49] Clark J.G., Bowden M.D. and Scannell R. 2021 Low temperature Thomson scattering on MAST-U *Rev. Sci. Instrum.* **92** 043545

[50] Reiter D. 2020 The data file AMJUEL: additional atomic and molecular data for EIRENE (available at: www.eirene.de/Documentation/amjuel.pdf)

[51] Myatra O., Lipschultz B., Moulton D., Verhaegh K., Dudson B., Orchard S., Fil A. and Cowley C. 2023 Predictive SOLPS-ITER simulations to study the role of divertor magnetic geometry in detachment control in the MAST-U Super-X configuration *Nucl. Fusion* **63** 096018

[52] Ahn J.W., Counsell G.F. and Kirk A. 2006 L-mode SOL width scaling in the MAST spherical tokamak *Plasma Phys. Control. Fusion* **48** 1077

[53] Verhaegh K. *et al* 2019 An improved understanding of the roles of atomic processes and power balance in divertor target ion current loss during detachment *Nucl. Fusion* **59** 126038

[54] Verhaegh K. *et al* 2024 Improved divertor performance in strongly baffled, alternative divertors on MAST Upgrade (arXiv:2311.08586)

[55] Verhaegh K. *et al* 2023 The role of plasma-atom and molecule interactions on power & particle balance during detachment on the MAST Upgrade Super-X divertor *Nucl. Fusion* **63** 126023

[56] Kukushkin A.S. and Krasheninnikov S.I. 2019 Bifurcations and oscillations in divertor plasma *Plasma Phys. Control. Fusion* **61** 074001

[57] Rozhansky V., Molchanov P., Veselova I., Voskoboynikov S., Kirk A. and Coster D. 2012 Contribution of drifts and parallel currents to divertor asymmetries *Nucl. Fusion* **52** 103017

[58] Hollocombe J. 2021 Cataloguing of ITER simulations using SimDB *Proc. 4th IAEA Technical Meeting on Fusion Data Processing, Validation and Analysis* (available at: https://conferences.iaea.org/event/251/contributions/20655/)

[59] Harrison J., Fishpool G., Thornton A. and Walkden N. (the MAST Team) 2015 The appearance and propagation of filaments in the private flux region in mega amp spherical tokamak *Phys. Plasmas* **22** 092508

[60] Walkden N., Harrison J., Silburn S., Farley T., Henderson S.S., Kirk A., Militello F. and Thornton A. 2017 Quiescence near the X-point of MAST measured by high speed visible imaging *Nucl. Fusion* **57** 126028